Journal of Constructional Steel Research 179 (2021) 106533

Contents lists available at ScienceDirect

Journal of Constructional Steel Research

Progressive collapse risk of 2D and 3D steel-frame assemblies having shear connections

Hussein Elsanadedy, Mohammed Alrubaidi, Husain Abbas, Tarek Almusallam, Yousef Al-Salloum *

Chair of Research and Studies in Strengthening and Rehabilitation of Structures, Dept. of Civil Engineering, College of Engineering, King Saud University, P.O. Box 800, Riyadh 11421, Saudi Arabia

ARTICLE INFO

Article history:
Received 9 September 2020
Received in revised form 30 December 2020
Accepted 7 January 2021
Available online xxxx

Keywords:
Progressive collapse
Steel beam-column connection
Column removal scenario
Catenary action
Simple connections
FE

ABSTRACT

In this research, the risk of progressive collapse of 2D and 3D single story one-third scale steel frame assemblies having shear beam-column connections was experimentally investigated under middle column loss event. The 2D assembly comprised two beams and three columns; whereas the 3D assembly was the same as the 2D assembly except with the addition of a transverse beam at the inner beam-column connection. A vertical quasi-static loading was placed on the middle column of the assembly in order to represent the event of progressive collapse. The two test frames together with another 2D steel frame assembly having simple joint, tested previously by other researchers, were employed to validate 3D finite element (FE) analysis created with the help of ABAQUS software. Thereafter, the calibrated models were utilized to study the progressive collapse risk for eight steel simple beam-column connections due to removal of the center column. Specimens were divided into two groups (4 specimens in each group), which were 2D and 3D steel frame assemblies. Behavior of different joints was numerically compared with respect to their failure modes and load versus displacement characteristics.

1. Introduction

Steel frame buildings are susceptible to progressive collapse when few structural elements (especially columns and beam-column joints) get damaged so that the neighboring structural members fail to redistribute the gravity loading. Thus, the limited damage can cause failure to adjacent members that may ultimately result in progressive collapse risk of the building. Examples of progressive collapse incidents of existing buildings are given in Refs. [1–7].

In various studies, the progressive collapse risk of 2D single story steel frame assemblies – comprising of two beams and three columns – was investigated. In a study by Khandelwal et al. [8], the progressive collapse risk of ten-story steel braced buildings, which were initially designed for seismic resistance, was numerically evaluated using the linear dynamic analysis of the alternate load path method. Kim and Kim [9] investigated numerically the progressive collapse potential of moment resisting steel frames by comparing the linear static and nonlinear dynamic analysis procedure of the alternate load path method. In a study by Kim and An [10], the influence of the catenary action phase on diminishing the progressive collapse risk in steel moment resisting frames was numerically evaluated using the nonlinear static analysis procedure. In another study by Grierson et al. [11], the equivalent spring approach was utilized to simulate the reduction in stiffness in the linear static analysis for assessment of progressive collapse risk of steel framed buildings.

A simplified methodology was suggested in Refs. [12, 13] to conduct the nonlinear static analysis for evaluating the progressive collapse risk of steel framed buildings. Lee et al. [14] offered a basic trilinear model to predict the collapse resistance of double span steel beams owing to column-loss events. In a study by Naji and Irani [15] the load-displacement and capacity curves of a fixed steel beam were utilized to model the progressive collapse potential of steel framed buildings. Elsanadedy et al. [16] assessed numerically the progressive collapse risk of an existing multi-story steel framed building under different blast scenarios using commercially available FE package [17].

In a study by Hadidi et al. [18], it was revealed that steel frames that are detailed for seismic resistance as per AISC-LRFD [19] cannot resist the risk of progressive collapse according to UFC guidelines [20]. Other researchers [21] concluded that the progressive collapse potential of a steel framed building is dependent on the analysis type and the column missing scenario. In another study by Zoghi and Mirtaheri [22], 3D nonlinear dynamic analysis was conducted to assess the progressive collapse risk of an existing steel framed building that was designed as per seismic codes taking into account the influence of infill wall panels. The energy approach was utilized by Chen et al. [23] to investigate the progressive collapse risk of steel buildings with moment resisting frames. It has been identified in some studies [24,25] that the flexure/axial force interaction in plastic hinges and

* Corresponding author.
E-mail address: ysalloum@ksu.edu.sa (Y. Al-Salloum).

https://doi.org/10.1016/j.jcsr.2021.106533
0143-974X/

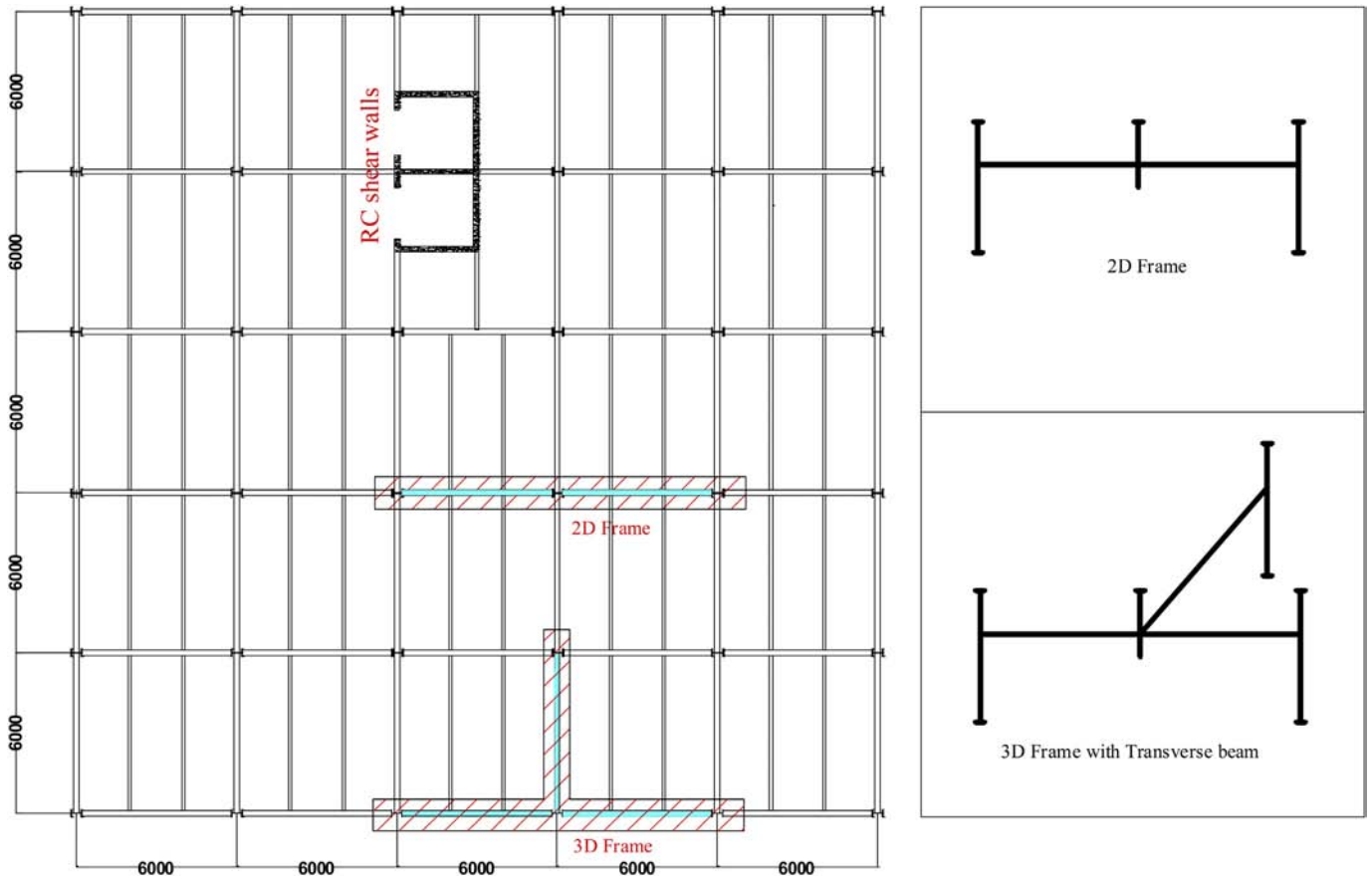

Fig. 1. Plan view of prototype building and selected specimens (Dimensions are measured in mm).

Table 1
Details of assemblies utilized for FE analysis validation[a].

Reference	Specimen ID	Column I-section $D \times B \times t_f \times t_w$ (mm)	Beam I-section $D \times B \times t_f \times t_w$ (mm)	Bolt	Size of shear plate /angle (mm)	Connection type
Current study	S-P-B-2D	200 × 200 × 12 × 8	194 × 150 × 9 × 6	Grade 10.9 M16	SP 120 × 100 × 6	Simple
	S-P-B-3D	200 × 200 × 12 × 8	194 × 150 × 9 × 6	Grade 10.9 M16	SP 120 × 100 × 6	Simple
Study of Yang and Tan [40]	S-W-C	216 × 206 × 17 × 10	304 × 165 × 10 × 6	Grade 8.8 M20	L 200 × 90 × 8	Simple

[a] D = depth of I-section; B = width of flange of I-section; t_f = thickness of flange of I-section; t_w = thickness of web of I-section; SP = shear plate; L = angle.

critical zones in steel frames has considerable reserve capacity owing to the strain hardening of beam sections. Different progressive collapse events of a steel framed building were investigated by Bae et al. [26]. The corner column removal was shown to be crucial for progressive collapse of part of the steel building. Macro-model was used by Han et al. [27] to investigate the progressive collapse potential of steel moment-resisting frames with stiffened beam-column joints. This modeling approach was able to simulate the joint deformation and the formation of catenary action stage in the progressive collapse event. In another study, stability considerations of steel frames subjected to corner column loss scenarios were emphasized by Gerasimidis et al. [28], where local inelastic column buckling or global system instability were identified as critical collapse mechanisms.

The influence of composite floor slabs on the progressive collapse risk of steel frames was numerically studied by several researchers [29–31]. Alashker et al. [29] investigated the progressive collapse potential of steel/concrete composite slabs in which the steel beams were connected to the columns via shear plates. Sadek et al. [30] developed finite element modeling for the composite slab by adding some modifications in modeling the shear studs. In another study, the progressive collapse risk of 3D steel frame assemblies without slabs was experimentally studied by Dinu et al. [32].

Qiao et al. [33] investigated the risk of progressive collapse of multistory steel framed structures by their simplification as single-story steel beam-column substructures. Naji [34] presented a simple modeling approach for assessing the progressive collapse risk of steel beam-column substructures due to middle column missing event. Ebrahimi et al. [35] investigated numerically the progressive collapse potential of six multistory steel moment frame buildings under column-loss events using 3D FE modeling. Two strengthening schemes for column-loss events were studied. These schemes included the use of

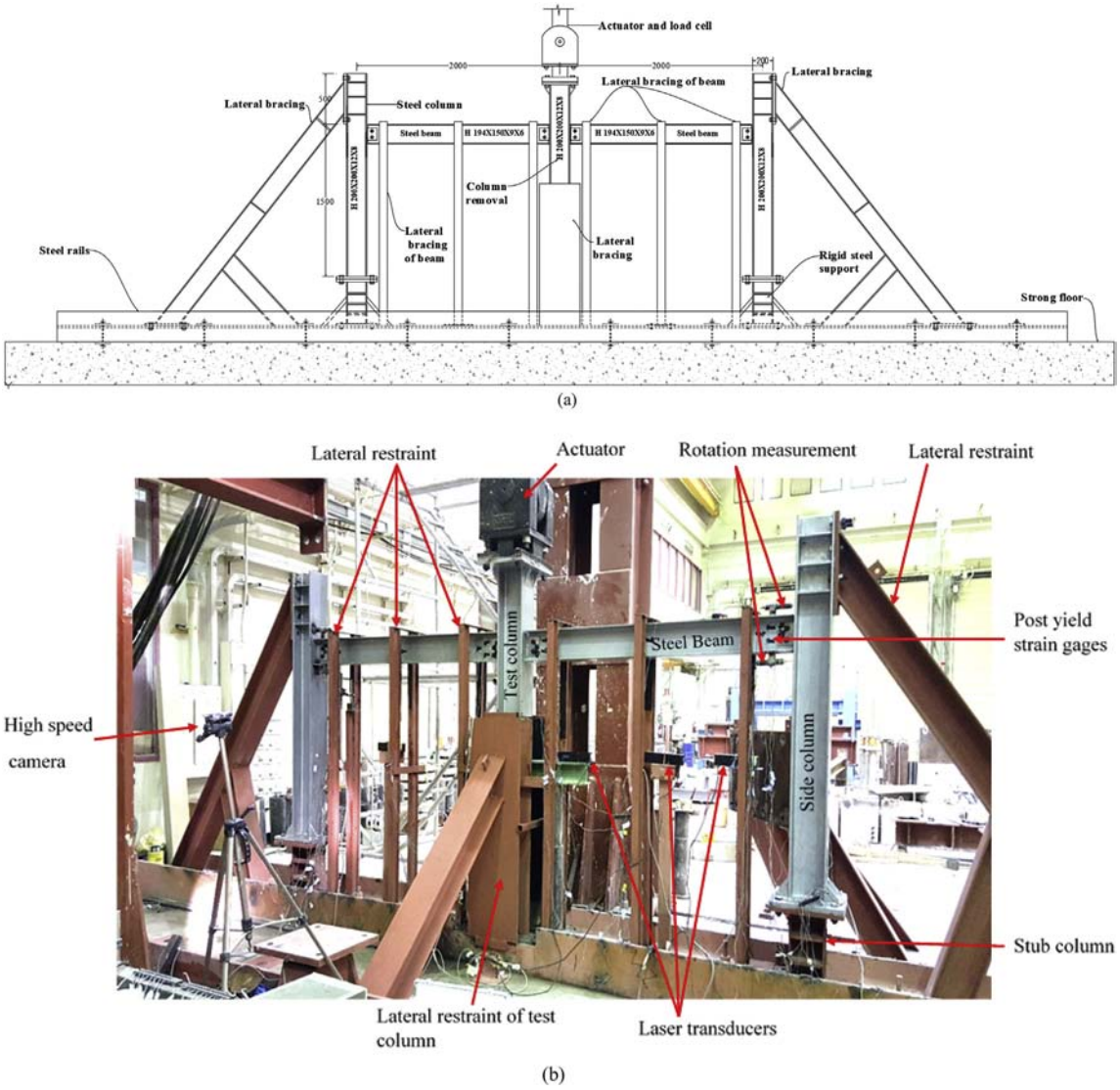

Fig. 2. Details of 2D assembly S-P-B-2D (Note: All dimensions are measured in mm): (a) Testing setup; (b) Instrumentation layout.

cables and braces. It is revealed that cables and bracing members could noticeably reduce the beam displacement at the missing column location. Foley et al. [36] performed linear dynamic analysis of 3D steel frames (after concluding that linear and nonlinear responses do not differ significantly), where slabs were replaced by horizontal stiffeners. Pantidis and Gerasimidis [37] developed analytical approach for assessing the robustness of 3D steel framed buildings subjected to an interior gravity column loss scenario. This approach was applied on a 9-story steel framed structure, and it was numerically verified. The developed analytical method was found to be in good agreement with the numerical results.

Alrubaidi et al. [38] presented experimental and numerical investigation on the behavior of different commonly used types of steel intermediate moment resisting frame joints under column-missing event. The authors found that tensile resistance of beam-column connections after experiencing large deformation generally controls the mode of failure and the development of catenary action. They also found that among all types of investigated beam-column connections, the one that was designed as per the Turkish-Earthquake Code [39] had the largest resistance against progressive collapse.

On the majority of the experimental and numerical studies, minimal consideration has been given to the influences of transverse beams, and especially, the additional capacity owing to transverse members. Therefore, a 3D beam-column assembly was experimentally evaluated in the current research to investigate the contribution of transverse beams in giving alternative load paths under column-loss event in simple steel beam-column connection. In this research, the progressive collapse risk of 2D and 3D single story one-third scale steel frame assemblies having simple shear beam-column joints was experimentally assessed under middle column missing event. The 2D assembly comprised two beams and three columns; while the 3D assembly was the same as the 2D assembly except with the addition of a transverse beam at the center beam-column connection. Progressive collapse was modeled by placing a quasi-static loading on the center column at a downward

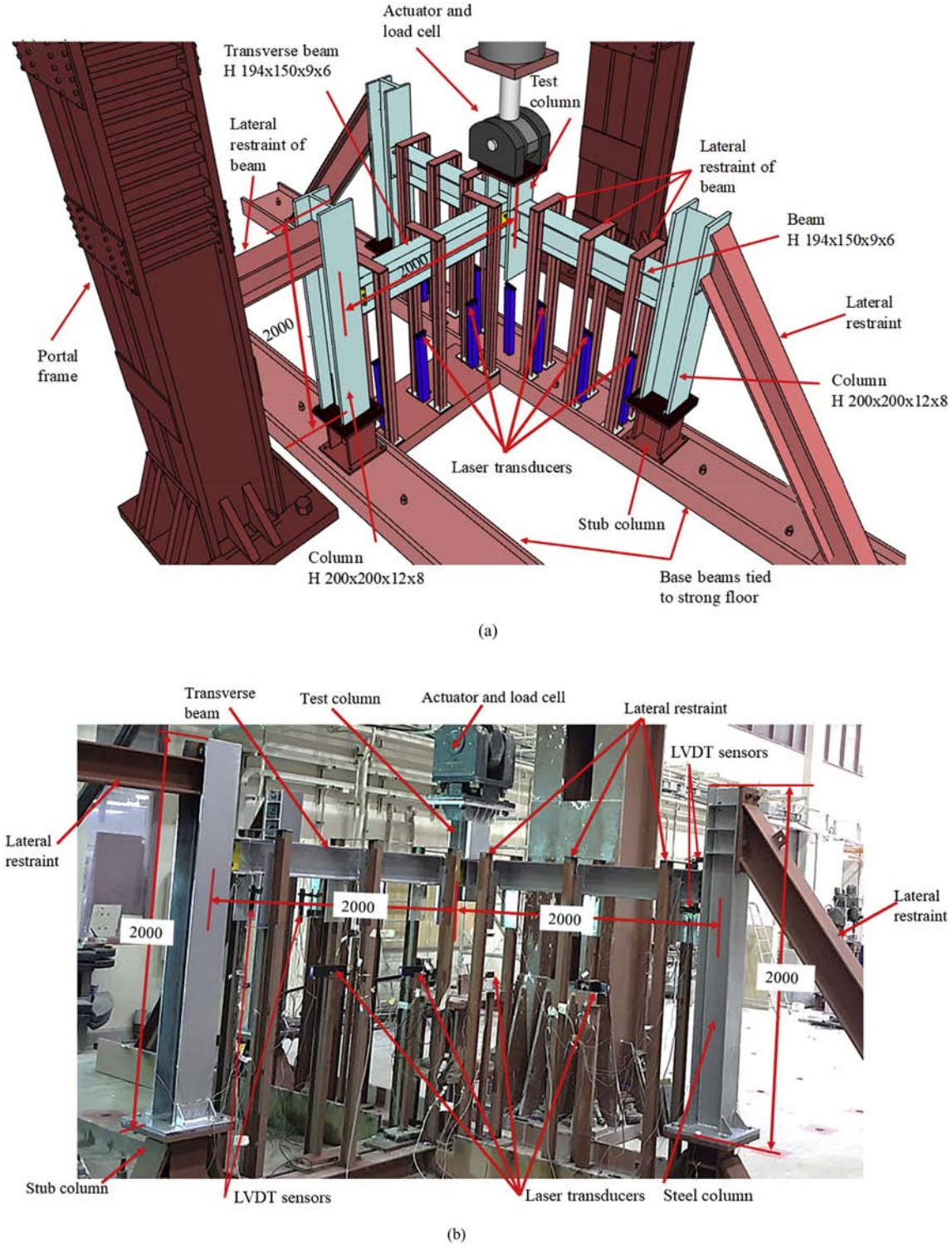

Fig. 3. Details of 3D assembly S-P-B-3D (Note: All dimensions are measured in mm): (a) Testing setup; (b) Instrumentation layout.

displacement rate of 100 mm/s. The two test frames along with another 2D steel frame assembly with simple beam-column connection, tested by Yang and Tan [40], were employed to validate 3D nonlinear FE models developed with the help of ABAQUS software [41]. These models considered the nonlinear material behavior with strain rate effects in addition to surface-to-surface contact algorithms between steel parts. Hence, the validated FE analysis was utilized to evaluate the progressive collapse potential of different steel simple beam-column connections. These connections were designed following the requirements of AISC-LRFD [42]. Behavior of simple beam-column joints was compared on the basis of their failure modes and load versus displacement characteristics at different stages.

2. Specimens and test setup

2.1. Design of Test Specimens

The two frame assemblies tested in the current research are one-third scale specimens of an eight-story prototype office steel building. The framing plan of the building in addition to the 2D and 3D assemblies are depicted in Fig. 1. The center-to-center spacing of columns in all directions was 6 m. Steel frames were taken out of the prototype building and they were then tested under middle column missing scenario. Details of the 2D and 3D test assemblies are given in Table 1 and Figs. 2 and 3. The 2D assembly (specimen S-P-B-2D) was prepared with shear-type beam-column joint and was employed as a control frame to be used as a baseline for comparison. The control frame assembly denotes one of the widely used steel beam-column connections in zones with non-seismic activity. The 3D assembly (S-P-B-3D) was designed to be the same as S-P-B-2D, except with the addition of a transverse beam at the center connection, as seen in Fig. 3. All frame assemblies have three columns with center-to-center spacing of 2 m with the total column height being 2 m (Figs. 2 and 3). Details of beam-column joints of the two test frames are shown in Fig. 4. Beams of all frame assemblies were constructed from the rolled steel section H 194 × 150, whereas the rolled steel section H 200 × 200 was utilized for columns, as presented in Table 1 and Figs. 2 and 3.

Fig. 4(a) depicts the single plate shear connection utilized in specimen S-P-B-2D. The beam web was connected to the 6-mm

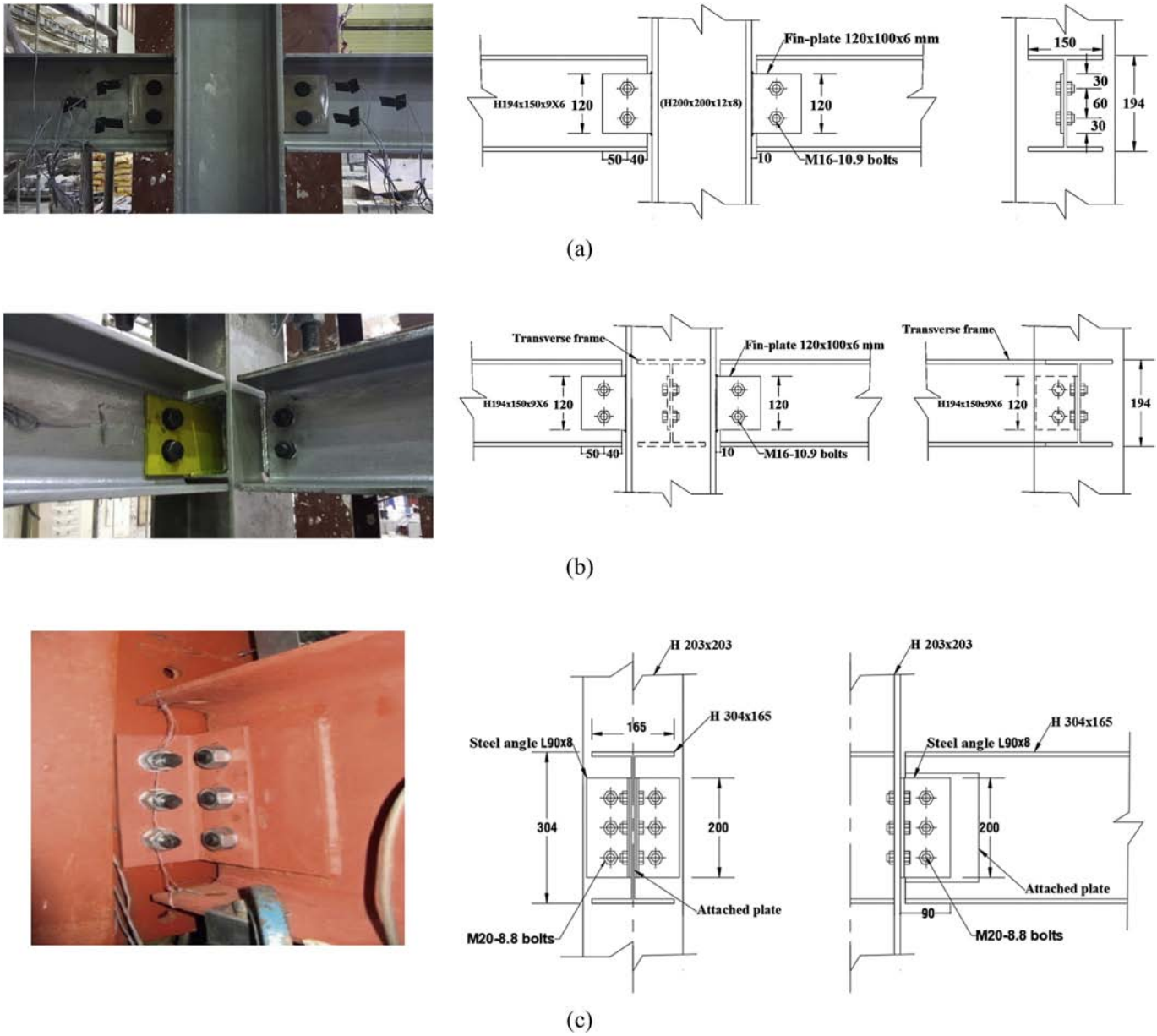

Fig. 4. Details of center connection of assemblies utilized for validating the FE analysis (Dimensions are measured in mm): (a) Assembly S-P-B-2D of this study; (b) Assembly S-P-B-3D of this study; (c) Assembly S-W-C tested by Yang and Tan. [40].

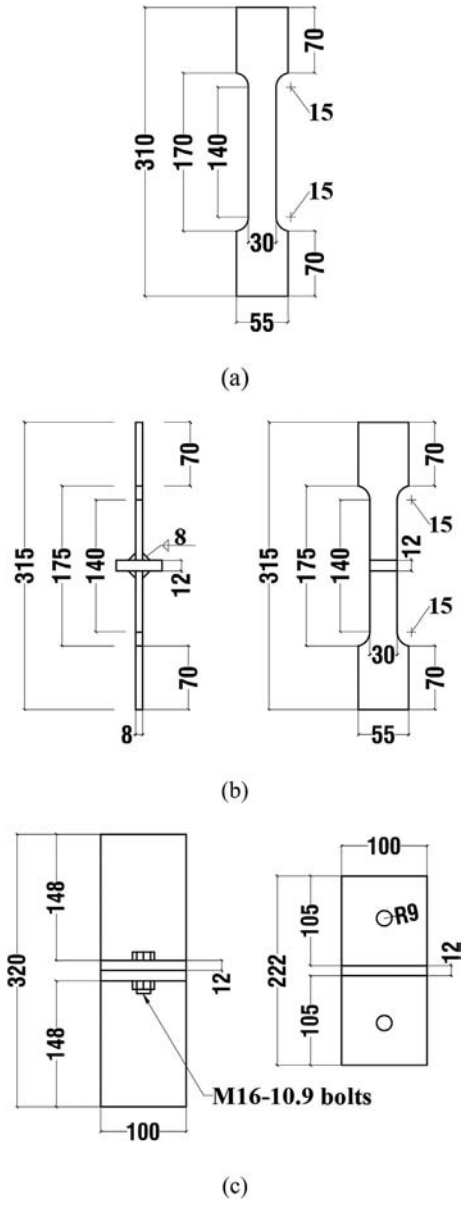

Fig. 5. Detailed size diagrams of the material characterization specimens (Note: All dimensions are measured in mm): (a) Coupon test; (b) Welded T-stub test; (c) Bolted T-stub.

thick tab plate using two M16, grade 10.9 bolts. Fillet welding was utilized to weld the tab plate to the flange of the column. The design of the welded connection followed the requirements of AISC-LRFD [42]. Figs. 3 and 4(b) show the 3D assembly S-P-B-3D. Besides the two frame assemblies tested in this research, another simple connection specimen (S-W-C) that was tested in literature by Yang and Tan [40] (see Table 1 and Fig. 4(c)) was employed for validating the FE analysis.

2.2. Properties of constituent materials

Prior to testing of specimens, standard steel coupons taken out of different parts (plates, beams and columns) were tested, for evaluating their mechanical properties. Additionally, the bolts and welding were tested using T-stub to determine their mechanical properties employed for validating the FE analysis (see Figs. 5 and 6). Tables 2 and 3 list measured material properties of different parts of test frames. It should be noted that the values shown in the Tables 2 and 3 are averages from three tests.

2.3. Instrumentation and test setup

For simulation of the real boundary conditions of the prototype building in the testing of specimens, the out-of-plane displacement at the level of the frame beams was restrained as presented in Figs. 2 and 3. Furthermore, the two exterior columns of the test specimen were partly extended above the level of the beam, and the upper ends of the columns were braced as shown in Figs. 2 and 3. It should be outlined that these bracings were designed to be stiff for simulating the continuity of columns and beams, respectively, in vertical and horizontal directions. It is worth mentioning here that the bracing system utilized in current study is the same as other previous studies [40,43–45].

In real progressive collapse events (especially due to blast threats), the column is removed abruptly with very high speed (strain rates in the range of 100–10,000 s^{-1} [46]). This abrupt column loss scenario was represented in the experiments by taking out the support of the middle test column and applying a vertical loading on that column using a high speed actuator at a rate of 100 mm/s. However, the very high speed in real progressive collapse events cannot be simulated in the tests owing to the actuator limits. The adopted loading rate (100 mm/s) was similar to quasi-static type testing, and it was found by the authors in prior studies [38,47–49] to have loads with strain rate of about 0.01 s^{-1}. Accordingly, the inertial effects in the tests were smaller than those expected in real progressive collapse events. Nevertheless, the increase in stresses due to the inertial forces is partially compensated by the increased material strength owing to strain-rate effect.

Test specimens were instrumented to record joint rotation, downward displacements, and strains in the critical locations. For accurate measurement of downward displacement of beams at different locations, laser transducers were utilized as seen in Figs. 2 and 3. Quasi-static loading was applied on the center column using an actuator in a displacement-controlled manner. Post-yield strain sensors were attached at crucial locations of connections to record strains in beams, as depicted in Figs. 2 and 3. Pretest FE models were developed with the help of ABAQUS [41] to assess approximately the behavior of test frames.

3. Experimental results

Table 4 lists the test results of the two frame assemblies tested in current research. The experimental results for specimen S-W-C tested by Yang and Tan [40] are also presented in the table. These results incorporate the vital parameters of the load-displacement curve, which are: (a) load at first yield of shear plate or angle at inner column face, (b) maximum loads of flexural and catenary action stages, (c) downward displacement of center column at first yield of shear plate or angle at inner connection, (d) downward displacements of center column at maximum loads of flexural and catenary action stages, (e) downward displacement of center column at ultimate state, (f) maximum axial force in the beam at catenary action stage, (g) dissipated energy (area under load-displacement curve) at ultimate state, (h) rotation of beam at maximum load, and (i) failure mode. It should be mentioned that the ultimate state is defined as that corresponding to a 20% reduction in the maximum load at the post-peak stage as per Ref. [50].

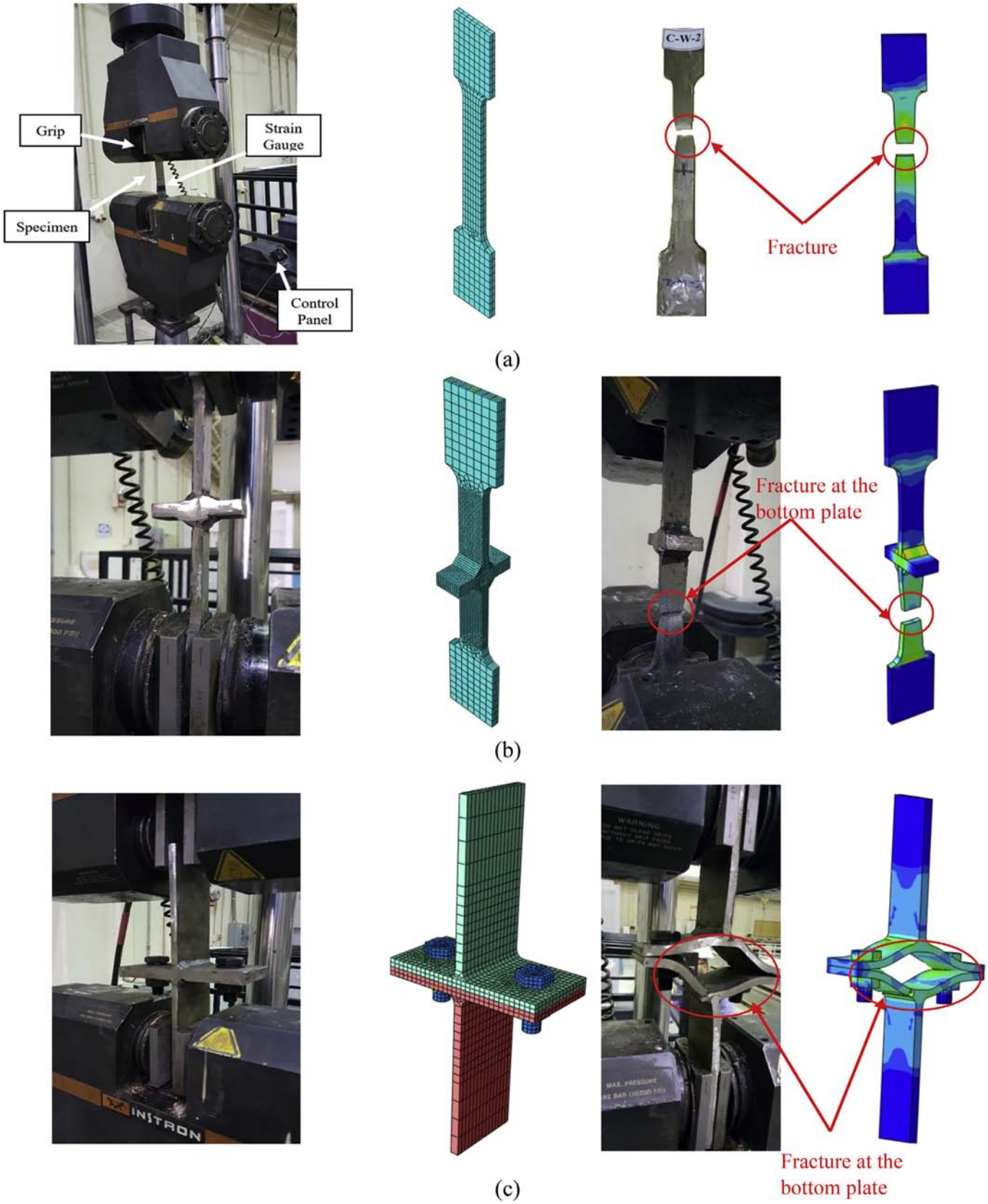

Fig. 6. Details of material specimens used for FE validation: (a) Coupon test; (b) Welded T-stub test; (c) Bolted T-stub test.

Table 2
Mechanical properties for material of different parts of assemblies tested in this study.

Component	Thickness t (mm)	Yield strength f_y (MPa)	Tensile strength f_u (MPa)	Elongation at fracture δ (%)
Column flange	12	295	466	22
Column web	8	304	462	20
Beam flange	9	332	471	23
Beam web	6	362	471	19
Shear plate	6	283	356	23
Bolt class 10.9	16	957	1071	10.3

For the 2D frame, in order to calculate the axial force in the beams $N_{u,CA}$, strain gages were employed to record the variation in axial strain along the beam depth. Consequently, distribution of normal stresses along the depth was calculated, and these stresses were integrated to compute the axial force in the beam. The rotations of ends of beams (θ) are assumed the same. The ultimate load of the frame assembly P_u comprises of two parts: load resistance owing to flexural action ($P_{u,FA}$) and load resistance due to catenary action ($P_{u,CA}$). Fig. 7 depicts the free body diagram of the 2D assembly. The two load components can be roughly assessed from the simple analysis proposed in Ref. [51] as per the following formulas:

$$P_{u,CA} = 2\,N_{u,CA}\,\sin\,\theta \tag{1}$$

$$P_{u,FA} = P_u - P_{u,CA} \tag{2}$$

For 3D frame, the free body diagram of the assembly is shown in Fig. 8. The peak load of the catenary action stage is computed from the simple analysis followed in Refs. [51, 52] as per the following formula:

$$P_{u,CA} = 3\,N_{u,CA}\,\sin\,\theta \tag{3}$$

The peak load at flexural action stage of the 3D frame assembly was then computed from Eq. (2). The maximum loads of flexural and catenary actions were then calculated for the three test specimens and are enlisted in Table 4. Below is a brief discussion of the experimental results for each test frame.

3.1. 2D simple connection (S-P-B-2D)

Depicted in Fig. 9(a) is the observed mode of failure for control frame S-P-B-2D. It is identified that steel buildings with simple shear connections are susceptible to the risk of progressive collapse under missing column event. As a typical characteristic of such connection, the beam rotation at ends is increased as the center column displacement is increased and the moment resisting capacity of the connection is limited. Load-displacement response of frame S-P-B-2D is shown in Fig. 9. As displayed in Fig. 10, the frame assembly could take small loading up to a displacement of 75 mm. At a displacement of 92 mm, tensile axial force was developed in the beam, which reveals the initiation of catenary action phase as shown in Fig. 10(b). Additional load increase resulted in bearing deformations of bolt holes in the tab plate. As the load was 72.6 kN, the tab plate at one of the outer joints fully fractured causing collapse of the assembly (see Figs. 9(a) and 10). The center column displacement at this stage was 386 mm (θ = 11.9°). The displacement profile of the beam at different loads is presented in Fig. 10(c).

3.2. 3D simple connection (S-P-B-3D)

As mentioned previously, a two-span beam and two exterior columns in the assembly plane connected to a transverse beam at the center connection was utilized for 3D simple connection S-P-B-3D. As

Table 3
Input parameters for material models used in the FE modeling.

Stage	Name of input parameter	Value of input parameter					
		Column flange	Column web	Beam flange	Beam web	Shear plate	Bolt class 10.9
Elastic	Young's modulus (GPa)	205	212	194	196	194	210
	Poisson's ratio	0.3	0.3	0.3	0.3	0.3	0.3
	Density (kg/m^3)	7.85×10^3	7.85×10^3	7.85×10^3	7.85×10^3	7.85×10^3	7.85×10^3
Plastic	True stress-strain curve	see Fig. 13(a)	see Fig. 13(a)	see Fig. 13(a)	see Fig. 13(a)	see Fig. 13(a)	see Fig. 13(b)
Damage of ductile	*Fracture strain*[a]	*0.55*	*0.56*	0.6	0.61	0.6	0.21

[a] Determined from the true stress-strain curves shown in Figs. 13(a) and (b).

Table 4
Key elements of experimental and FE load-displacement response[a]

Specimen ID	Results	Flexural action stage				Catenary action stage				P_u (kN)	Δ_u (mm)	E_u (kN.m)	θ (degree)	Mode of failure
		P_y (kN)	Δ_y (mm)	$P_{u,FA}$ (kN)	$\Delta_{u,c\text{-}FA}$ (mm)	$P_{u,CA}$ (kN)	$P_{u,CA}$ / $P_{u,FA}$	$\Delta_{u,c\text{-}CA}$ (mm)	$N_{u,CA}$ (kN)					
S-P-B-2D	EXP	–	–	9	92	72.6	8.07	375	172	72.6	386	12.5	11.9	Fracture of tab plate
	FE	–	–	9	92	71.5	7.94	383	172	71.5	383	12.7	11.8	
	EXP/FE	–	–	1.00	1.00	1.02	1.02	0.98	1.00	1.02	1.01	0.98	1.01	
S-P-B-3D	EXP	–	–	10.8	77	116	10.7	404	204	116	500	28.2	11.4	Fracture of tab plate
	FE	–	–	13.1	77	115	8.7	400	201	115	503	28.3	11.1	
	EXP/FE	–	–	0.82	1.00	1.00	1.2	1.01	1.01	1.00	0.99	1.00	1.02	
S-W-C	EXP	–	–	3	75	119	40	367	369	119	385	14.6	8.97	Angle fracture
	FE	–	–	3	74	120	40	367	367	115	374	14.5	8.6	
	EXP/FE	–	–	1.00	1.01	0.99	1.00	1.00	1.00	1.03	1.03	1.00	1.04	

[a] P_y = load at first yield of plate or angle at inner column face; Δ_y = displacement of middle column at first yield of plate or angle at inner column face; $P_{u,FA}$ = peak load of flexural action stage; $\Delta_{u,c\text{-}FA}$ = displacement of middle column at peak load of flexural action stage; $P_{u,CA}$ = peak load of catenary action stage; $\Delta_{u,c\text{-}CA}$ = displacement of middle column at peak load of catenary action stage; $N_{u,CA}$ = peak beam axial force at catenary action stage; P_u = progressive collapse resistance; Δ_u = displacement of middle column at ultimate state; E_u = energy dissipated at ultimate state; and θ = beam rotation at maximum load.

shown in Fig. 11, behavior of this connection was much better than the 2D assembly S-P-B-2D with regard to flexural stiffness and progressive collapse resistance. Furthermore, as identified from Table 4, the rotation of specimen S-P-B-2D under column-missing event is almost same as rotation of specimen S-P-B-3D. From Figs. 10 and 11, it is clear that the initial response of S-P-B-3D specimen up to a displacement of 75 mm is almost same as specimen S-P-B-2D. For 3D assembly S-P-B-3D, tensile axial force in the beam was initiated at a displacement of 77 mm, which reveals the initiation of the catenary action phase as shown in Fig. 11(b). Additional load increase resulted in bearing deformations of bolt holes in the tab plate. As the load was 116 kN, tab plates at the middle beam-column joint (where it is connecting to transverse beam) fully fractured causing collapse of the test assembly as seen in Figs. 9(b) and 11. At this stage, the center column displacement was 404 mm ($\theta = 11.4°$). The displacement profile of the longitudinal beams at different loads is presented in Fig. 11(c).

4. FE analysis

The commercial FE package ABAQUS [41] was utilized to model test frames. Accounting for its symmetry, only one-half of the assembly was modeled. Details of the FE modeling are discussed below.

4.1. FE mesh

Fig. 12(a) presents the FE geometry for frame S-P-B-3D. Eight-node constant stress brick elements were used for different parts (columns, beams, tab plates, bolts, stub columns, and lateral restraints for beams

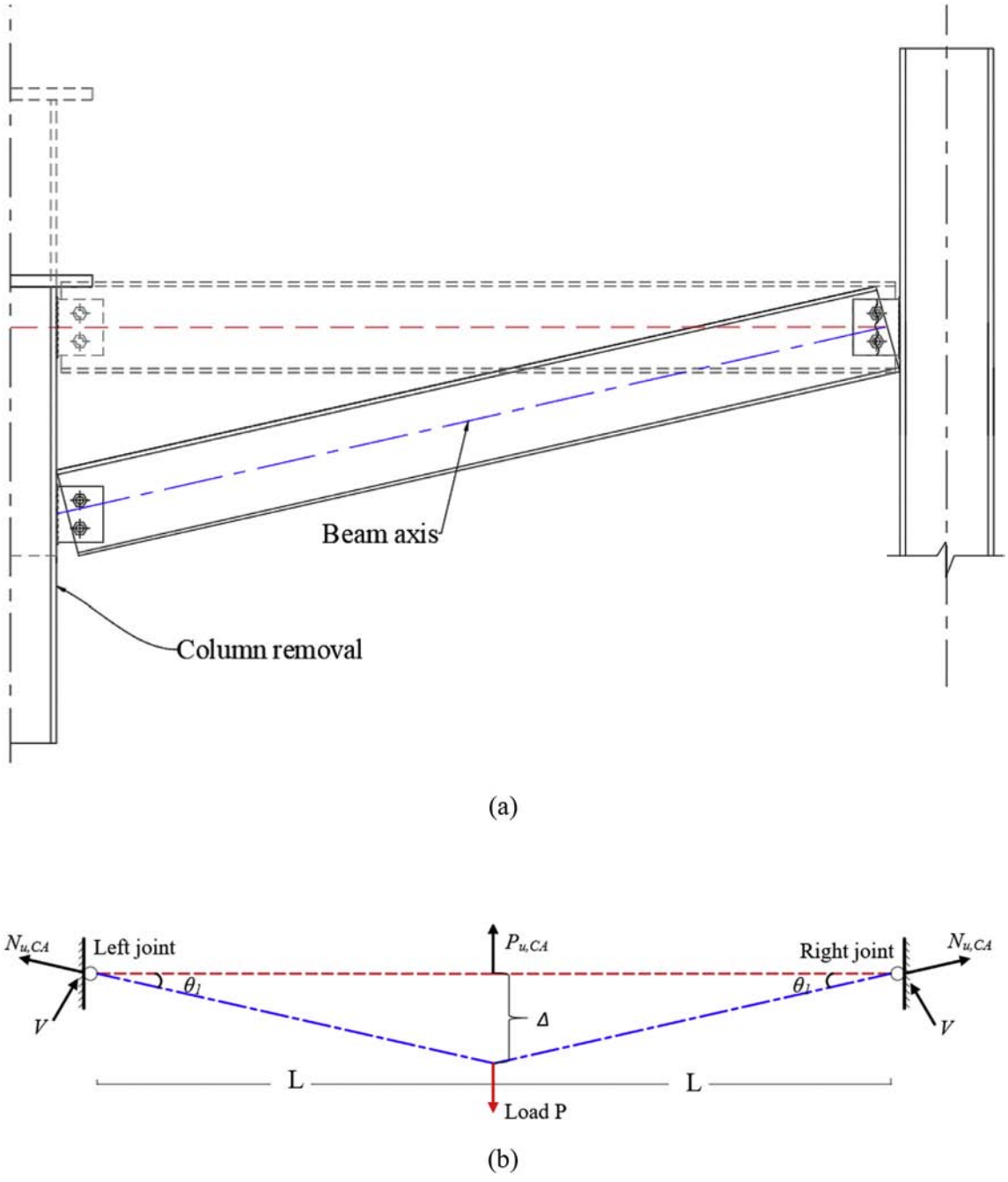

Fig. 7. 2D simplified mechanical model: (a) Deformed shape of 2D specimen; (b) Force equilibrium diagram for the catenary action stage.

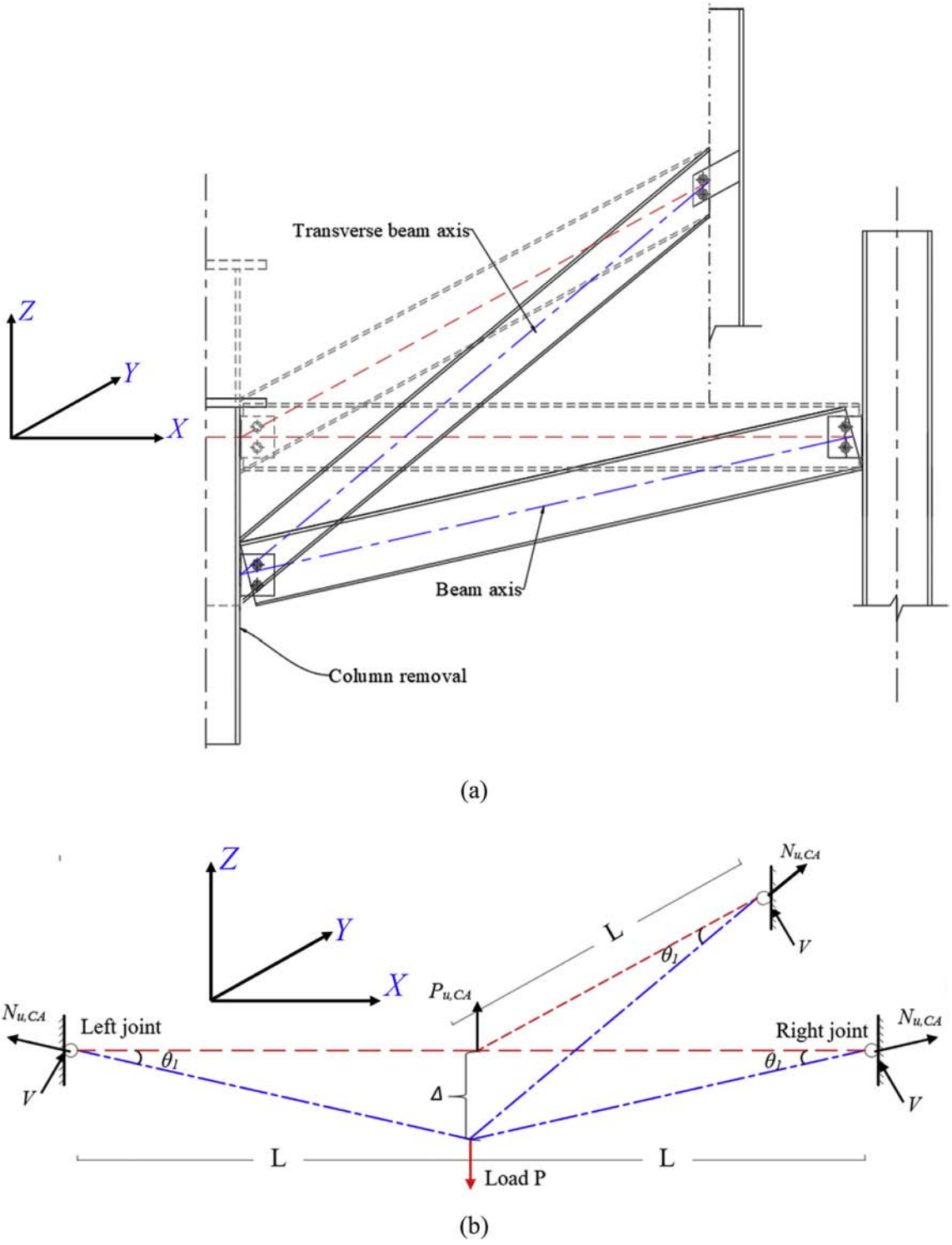

Fig. 8. 3D simplified mechanical model: (a) Deformed shape of 3D specimen; (b) Force equilibrium diagram for the catenary action stage.

and columns). The size of brick elements in the FE mesh varied from 2 to 25 mm. For bolts, a dense mesh with 2.0 mm size was employed. However, element size was about 5 mm at beam ends, where fracture of tab plates occurred (Fig. 12(b)). It is worth mentioning here that a mesh sensitivity analysis was conducted and it was realized that a further mesh refinement would have slight impact on the FE results; however, it will significantly increase the computational time.

4.2. Material model calibration

Table 3 lists the input parameters for material models used in the FE modeling. For material model input parameters listed in Table 3, tensile tests were conducted on standard steel coupons (welded T-stub and bolted T-stub) as per relevant standards in Ref. [53]. The output of each tensile test is the engineering stress-strain (σ_E - ε_E) curve, which

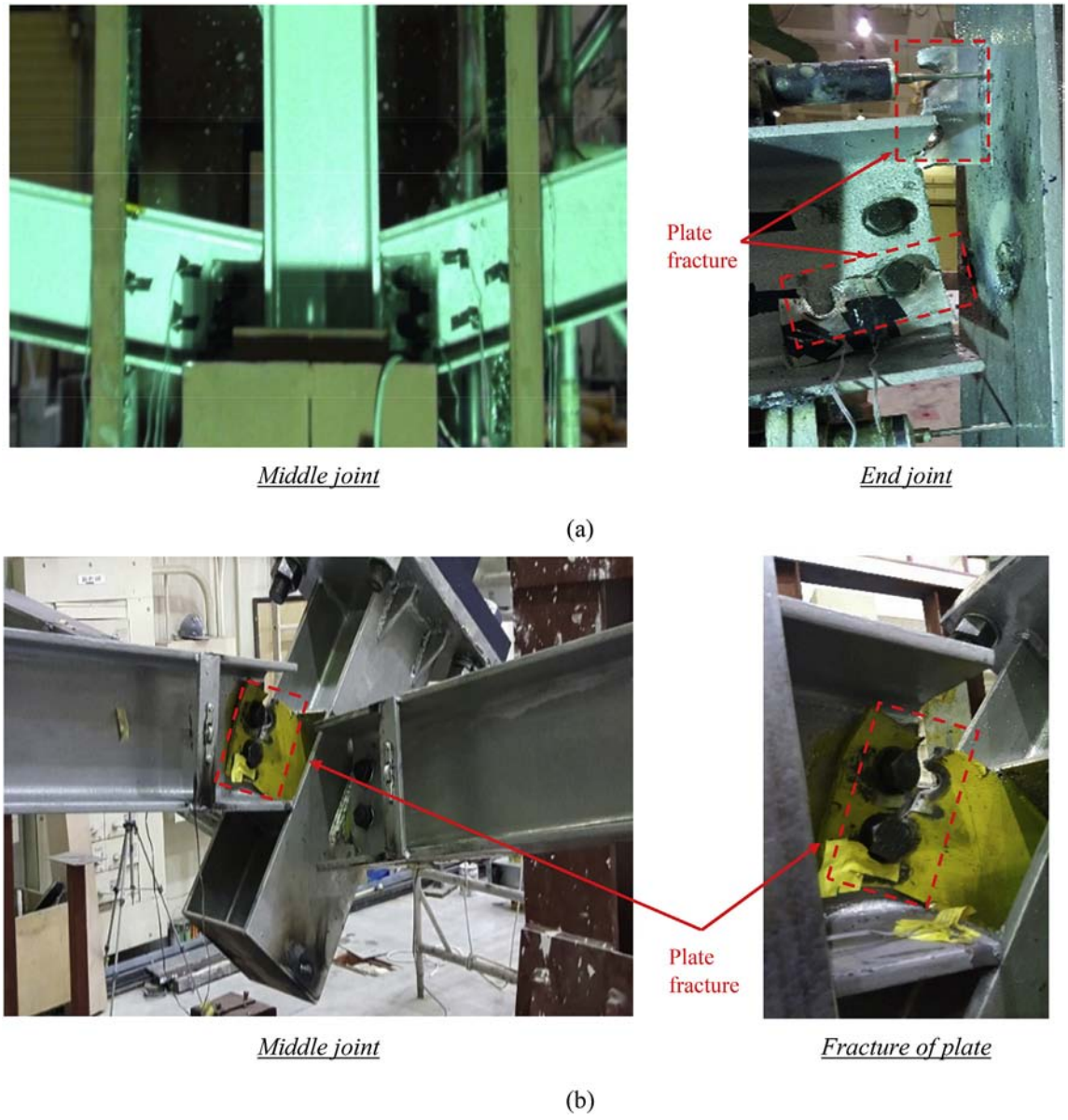

Fig. 9. Experimental failure mode for assemblies of this study: (a) Assembly S-P-B-2D; (b) Assembly S-P-B-3D.

was converted into a true stress-strain (σ_{true} - ε_{true}) curve (Fig. 13) using the following Eqs. [54]:

$$\sigma_{true} = \sigma_E(1 + \varepsilon_E) \tag{4}$$

$$\varepsilon_{true} = \ln(1 + \varepsilon_E) \tag{5}$$

For standard steel coupons, once they reach their peak load, owing to necking, they appear to soften, whereas they are really hardening [55,56]. The true stress-strain plot (Fig. 13) past the peak strength of the engineering stress-strain relationship was taken ascending with a parabolic shape. FE models were created in ABAQUS [41] for the tensile test of steel coupons, using the actual dimensions of the coupon specimens (Figs. 5 and 6). In this regard, 8-noded solid elements were employed and the element size was calibrated by iterative analysis. The size of the FE mesh was adjusted until quantitative agreement of the measured and calculated load-displacement curves for the three coupon types as seen in Fig. 14. The experimentally observed steel fracture in the coupons was simulated by element deletion using the "damage for ductile metal" approach available in ABAQUS [41]. In this approach, elements were eroded from the FE model using the plastic fracture strain (listed in Table 3) determined from the true stress-strain curves shown in Fig. 13 for different parts. Fig. 6 shows comparison between the experimental and FE failure modes for samples of the standard tests on steel coupons, welded T-stubs, and bolted T-stubs. Good agreement was noticed between the experimental and FE results. This confirms the aptness of both element size and input material parameters in capturing steel fracture via element erosion. Thus, the calibrated element size has been used in the 3D FE modeling of the 2D and 3D frame assemblies, especially at critical locations near beam-column connections.

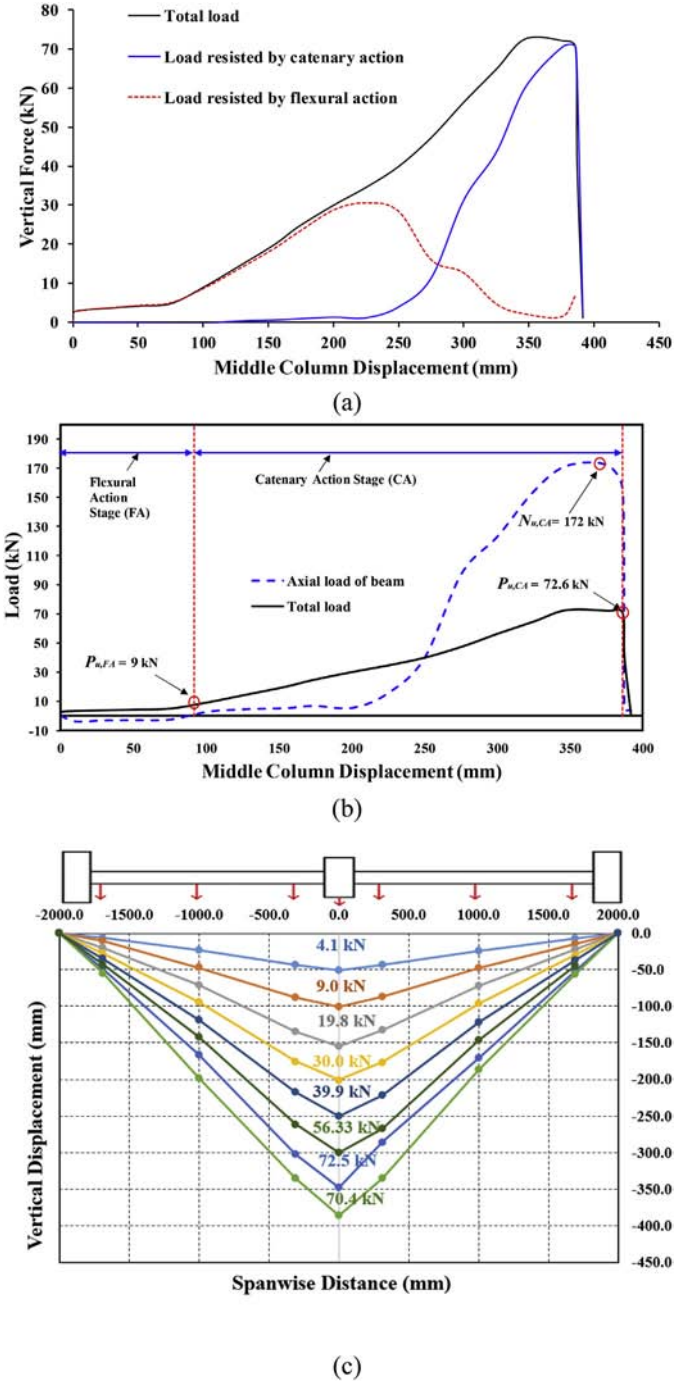

Fig. 10. Load vs displacement relationship for assembly S-P-B-2D of this study: (a) Envelope of load vs displacement; (b) Flexural and catenary action phases; (c) Displacement profile of beam at different load levels.

4.3. Boundary conditions and loading strategy

As displayed in Fig. 12, the modeled boundary conditions represented precisely those of the test specimens. Supports at base of columns as well as lateral bracing were modeled at the same locations as the tests (Fig. 12). For more accurate modeling of the boundary conditions, the actual stiffness of the lateral bracing members was represented by their modeling using solid elements. However, both stub columns and bracing members were rigidly connected to base steel I-beams, which were tied to the strong floor of the lab. Accordingly, the bases of the stub columns and bracing members were modeled as fixed supports, as seen in Fig. 12(a). The out-of-plane movement of the flanges of the beam was restrained at the nodes where lateral bracing members are added in the test assembly. As presented in Fig. 12, the fixity of the base of outer columns was modeled via restraining rotation and displacement at the lower end nodes in the global Cartesian coordinates.

The explicit module of ABAQUS was employed to conduct the FE modeling. This has been validated in prior studies on progressive

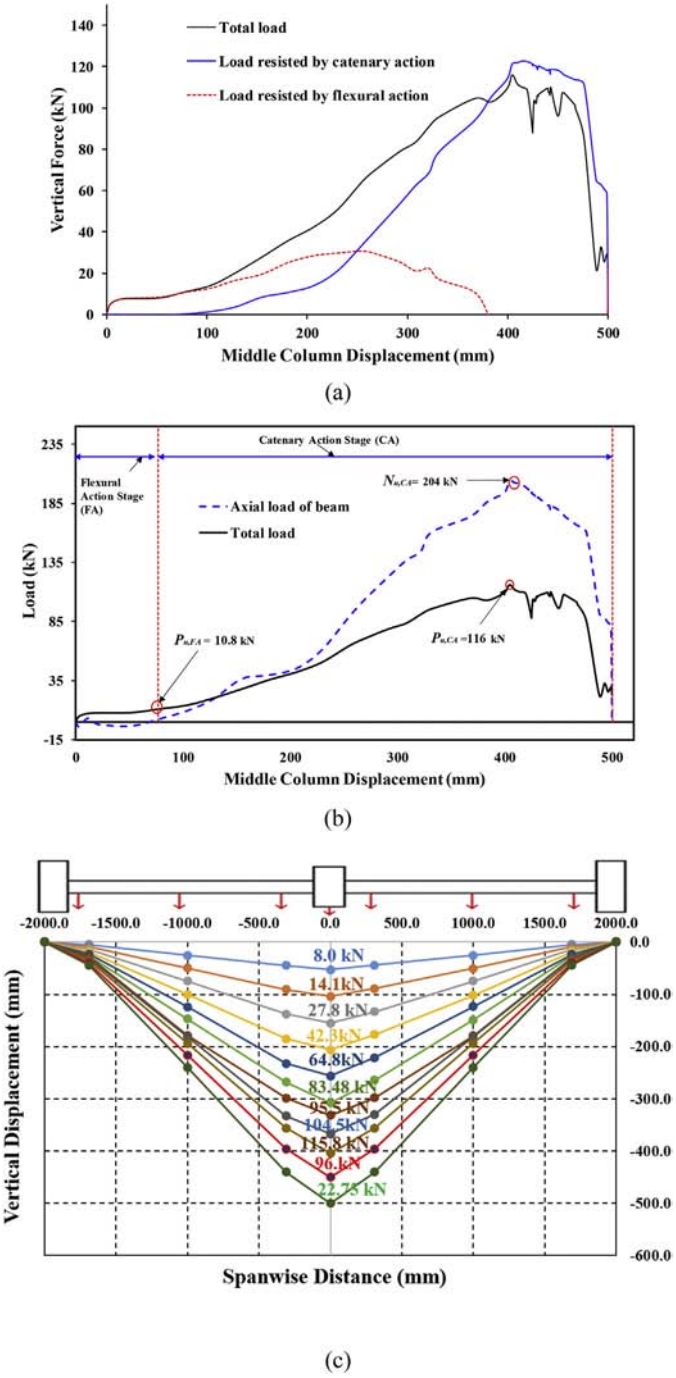

Fig. 11. Load vs displacement relationship for assembly S-P-B-3D of this study: (a) Envelope of load vs displacement; (b) Flexural and catenary action phases; (c) Displacement profile of beam at different load levels.

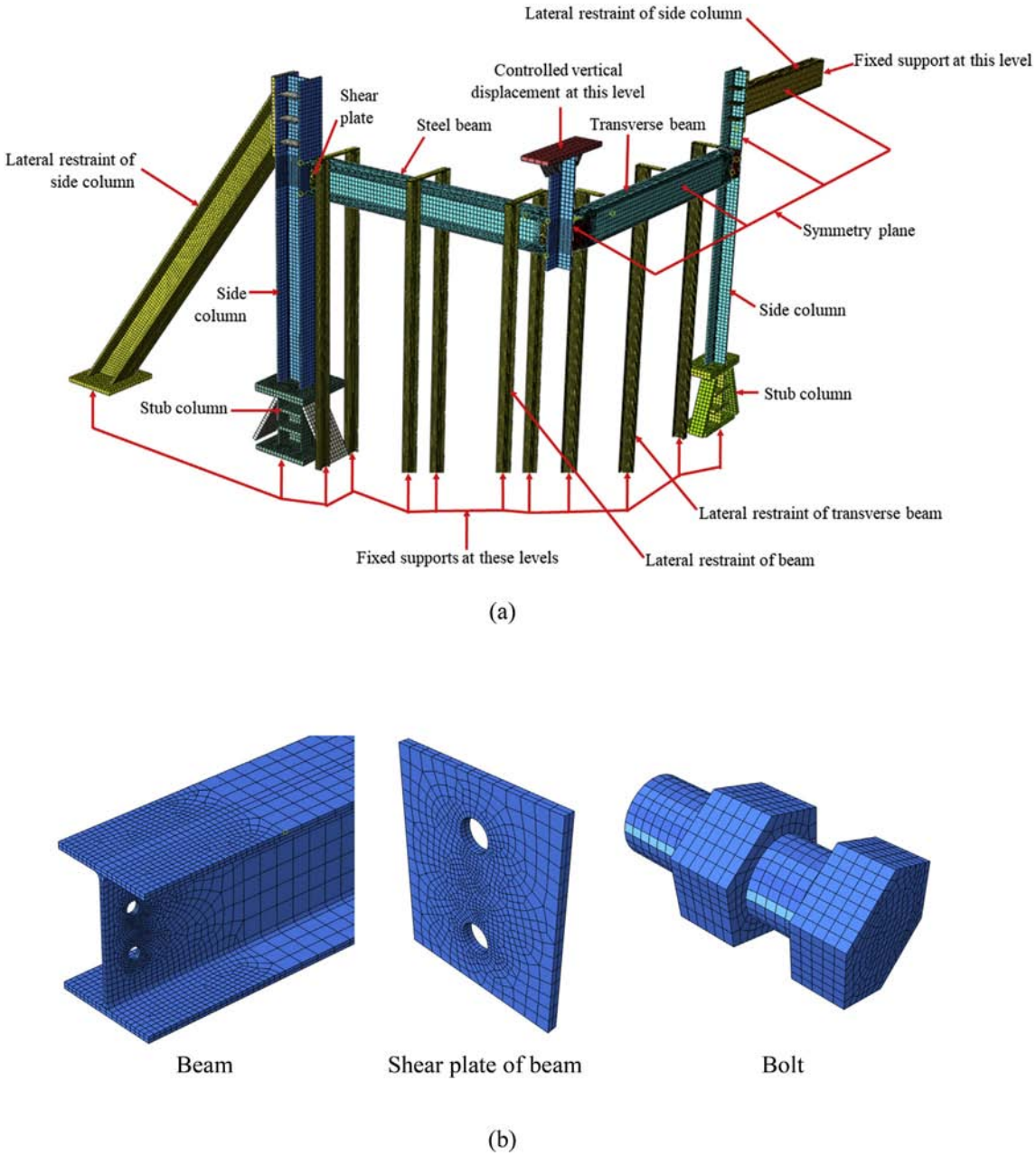

Fig. 12. FE mesh for assembly S-P-B-3D: (a) Overall view; (b) View of different parts.

collapse of buildings [38,44,57]. Owing to symmetry in the specimens, only one-half of the assembly was modeled, as displayed in Fig. 12(a), and boundary conditions simulating symmetry were input in the model. In order to model the displacement-controlled quasi static loading used in the experiments, displacement versus time function was input to the upper end nodes of the center column. The general contact type of ABAQUS software was input between elements of webs, bolts, and tab plates. A friction coefficient of 0.3 was input for the steel elements that were firstly in contact [41,47]. The welding between different steel parts was modeled using "tie" contact interface [41].

4.4. Validation of FE analysis

The test results of the two assemblies of current study (S-P-B-2D and S-P-B-3D) in addition to specimen S-W-C tested by Yang and Tan [40] were employed to validate the FE modeling. Discussion of the FE modeling results is presented with regard to failure mode and load-displacement response.

Table 4 lists comparison between experimental and FE key results of load versus displacement response for the three test assemblies. As depicted from Table 4, errors in the prediction of maximum load of flexural and catenary actions ranged from 0%–18% and 0%–2%, respectively. In addition, prediction errors of 0%–1% and 0%–2% were, respectively, estimated for middle column displacement at maximum load of flexural and catenary actions. However, the error in the prediction of maximum axial force in the beam at catenary action stage ranged from 0%–1%. Moreover, it is noted from Table 4 that the dissipated energy was well estimated by the FE analysis with error in prediction ranging from 0%–2%.

Fig. 15 displays the FE modes of failure of the three test frames and it is clarified that they match well with the test observations. Figs. 16

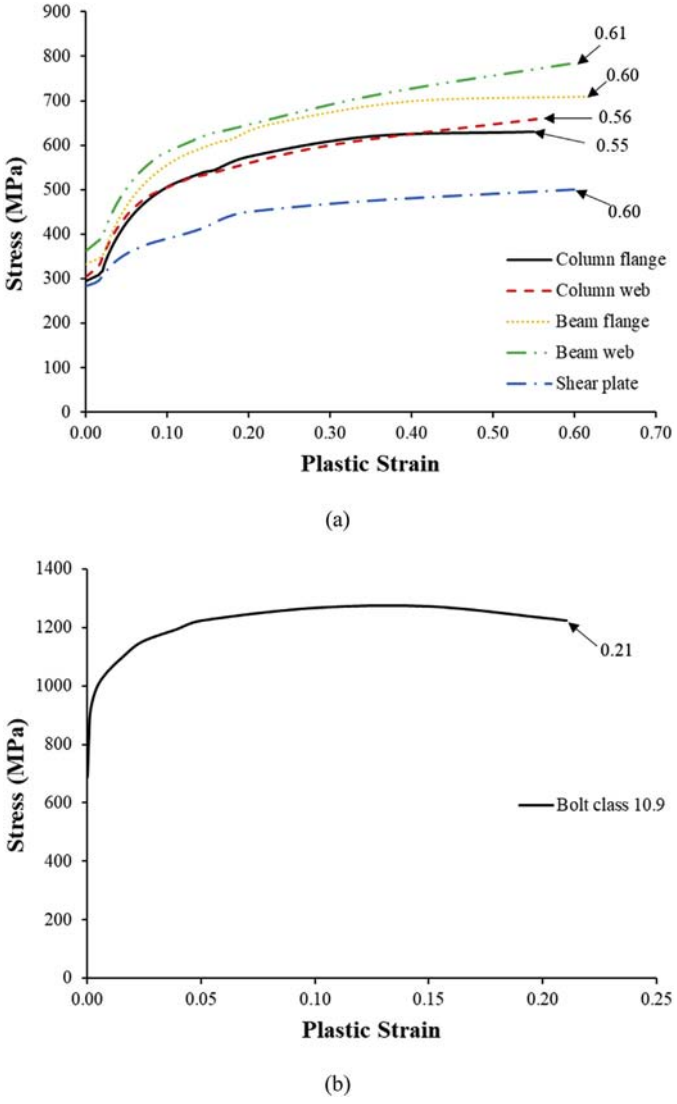

Fig. 13. True stress vs plastic strain graph for (a) Coupon materials; (b) 10.9 bolt material.

(a) to (c) illustrate comparisons between experimental and FE load-displacement curves for the three specimens. Good agreement was obtained between the two envelopes, particularly for the peak load. Moreover, as seen from Figs. 16(a) to (c), the stiffness of the specimens was well predicted in the FE modeling. Also, the descending part of the load versus displacement curve was well estimated in the FE analysis as presented in Figs. 16(a) to (c). This evidences the accuracy of the constitutive models used in the analysis. Thus, the developed FE analysis was validated for steel shear beam-column joints. Therefore, the validated models can be employed in the assessment of progressive collapse potential of different designs of steel simple beam-column joints under column-missing events, as will be detailed in the following section.

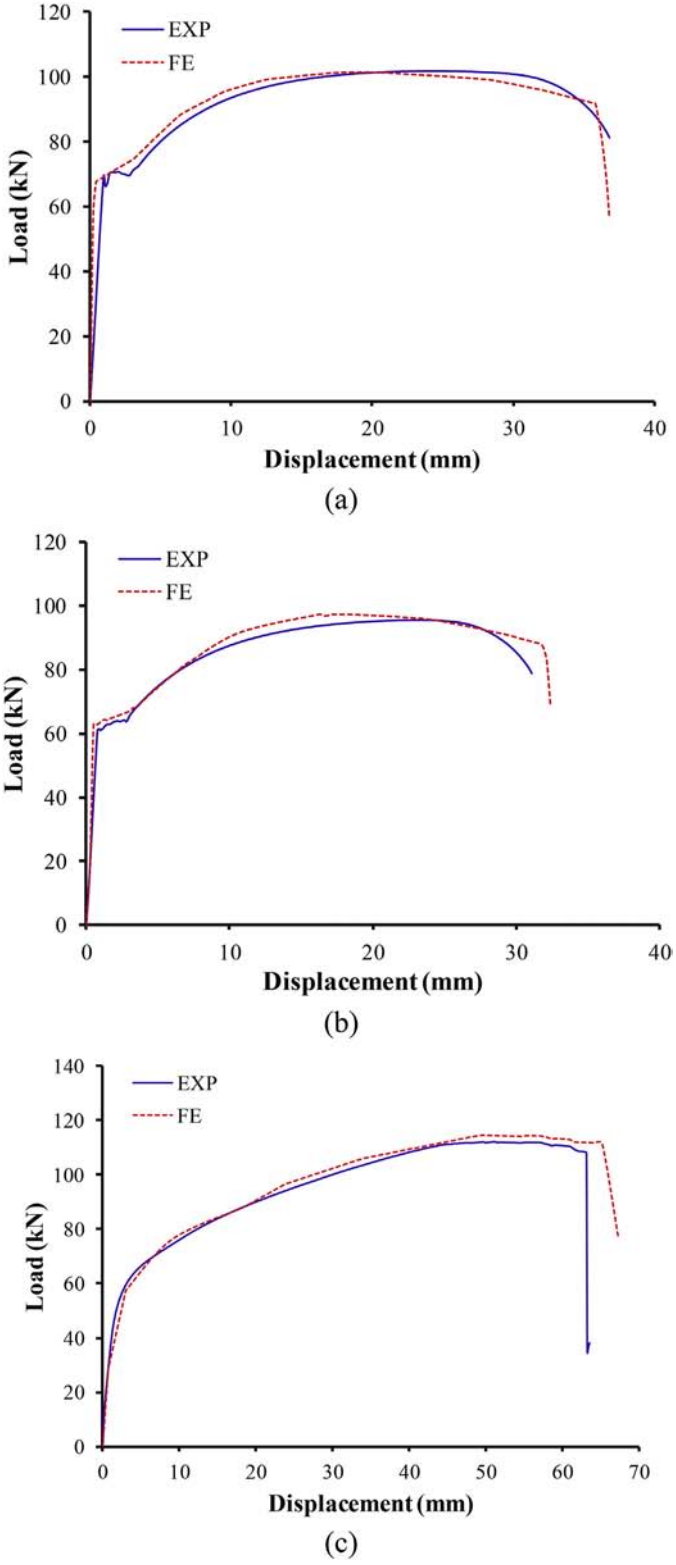

Fig. 14. Comparison of load vs displacement response for: (a) Coupon plate specimen; (b) Welded T-stub specimen; (c) Bolted T-stub specimen.

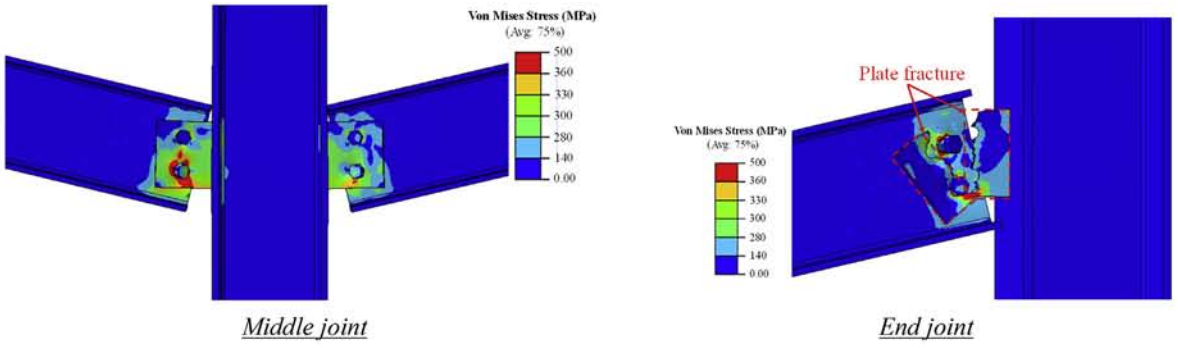
Von Mises Stress (MPa)
(Avg: 75%)
500
360
330
300
280
140
0.00
Plate fracture
Middle joint
End joint

(a)

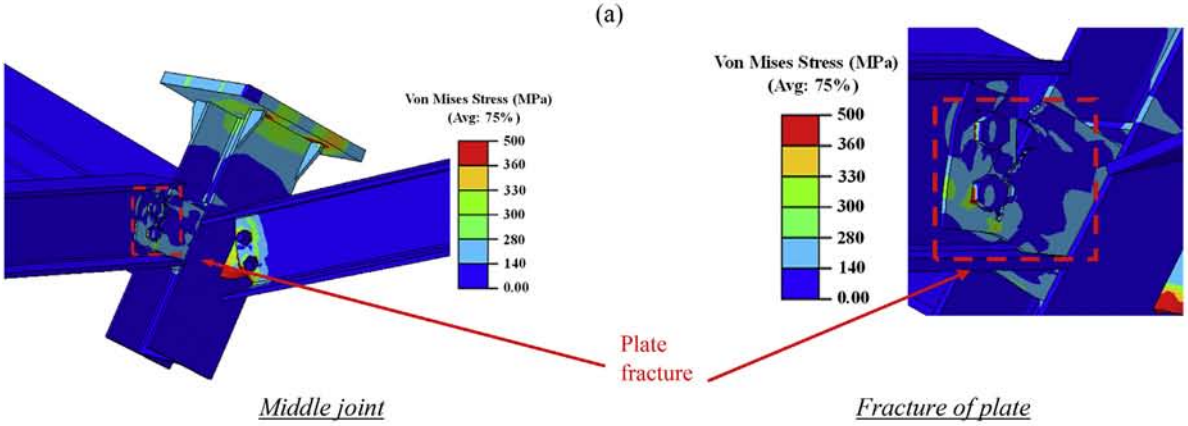
Von Mises Stress (MPa)
(Avg: 75%)
500
360
330
300
280
140
0.00
Plate
fracture
Middle joint
Fracture of plate

(b)

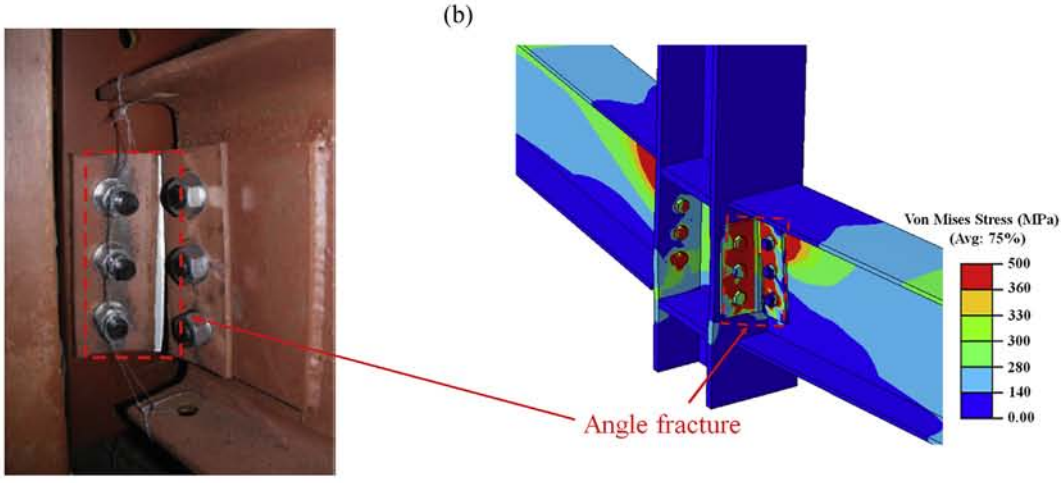
Von Mises Stress (MPa)
(Avg: 75%)
500
360
330
300
280
140
0.00
Angle fracture
Experimental
FE

(c)

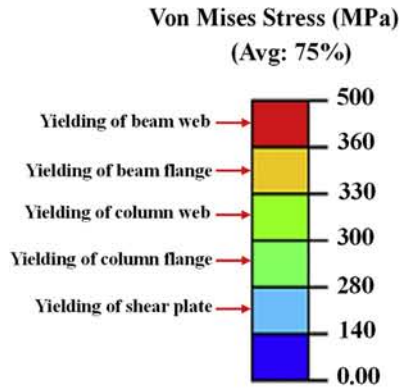
Von Mises Stress (MPa)
(Avg: 75%)
Yielding of beam web
Yielding of beam flange
Yielding of column web
Yielding of column flange
Yielding of shear plate
500
360
330
300
280
140
0.00

(d)

5. FE study of different shear joints

Eight simple beam-column joints were studied using FE modeling under center column-missing events as presented in Table 5 and Fig. 17. These joints were designed according to AISC-LRFD [42]. As explicable from Table 5 and Fig. 17, out of the eight assemblies, two joints have single shear plate welded to column flange and beam web, whereas six joints have double angle bolted (or welded) to column flange and beam web. As shown in Table 5, these joints, specifically, are: S-P-W-2D (single shear plate welded to column flange and beam web), S-P-W-3D (same as S-P-W-2D but with transverse beam), D-A-B-2D (double angle bolted to column flange and beam web), D-A-B-3D (same as D-A-B-2D but with transverse beam), D-A-W-2D (double angle welded to column flange and beam web), D-A-W-3D (same as D-A-W-2D but with transverse beam), D-A-B-W-2D (double angle bolted to beam web and welded to column flange), and D-A-B-W-3D (same as D-A-B-W-2D but with transverse beam). It is worth noting that specimen S-P-W-2D is identical to specimen S-P-B-2D, which has been tested in current research, but with shear plate welded to flange of column and web of beam, as shown in Fig. 17(a).

FE modes of failure for the eight studied simple connections are illustrated in Fig. 18. Key elements of load versus displacement characteristics are listed in Table 6 for the eight connection specimens. Figs. 19 to 26 display FE load-displacement curves for all eight specimens. Discussions of the FE analysis results of different simple connections are detailed below.

5.1. Welded single shear plate connections

Load versus displacement relationship for specimen S-P-W-2D is presented in Fig. 19. Throughout the preliminary loading phase, the behavior of the specimen was nearly in the linear elastic stage without obvious damage. Following the initial yielding of the tab plate, the load-displacement response was nonlinear with reduction in the secant stiffness. Specimen S-P-W-2D had significant displacements and rotations prior to its failure. At a center column displacement of 194 mm, the welded tab plate of the exterior connection fractured, and then it fully separated from the exterior column flange (Fig. 18(a)). The predicted load at this displacement level was about 81 kN and the rotation of the beam was nearly 5.5° (Table 6).

Fig. 20 shows load-displacement curve for specimen S-P-W-3D. During the preliminary loading phase, the behavior of the specimen was nearly in the linear elastic stage without obvious damage. Following the initial yielding of the tab plate, the load-displacement response was nonlinear with reduction in the secant stiffness. It is noted that prior to its failure, specimen S-P-W-3D had larger rotation and displacement than specimen S-P-W-2D. Failure of specimen S-P-W-3D was at a middle column displacement of about 257 mm that is correspondent to a peak load of about 151 kN and a beam chord rotation of almost 7.3°. Failure of specimen S-P-W-3D was because of fracture of the tab plates at the middle beam-column joint. As illustrated in Fig. 18(b), this fracture propagated through the plates until the specimen was not able to carry additional loading.

5.2. Double angle connections

Load versus displacement relationship of specimen D-A-B-2D is shown in Fig. 21. Due to the limited moment capacity of the simple shear connection, the frame assembly rotated at both ends with increasing center column displacement. During the preliminary loading phase, the specimen was not able to carry any loading until tensile axial force was developed in the beam at large displacement. This reveals the onset of the catenary action stage as illustrated in Fig. 21. As shown in Fig. 21 and Table 6, the specimen reached its maximum load of flexural action phase (9 kN) at a displacement of 102 mm. At this displacement

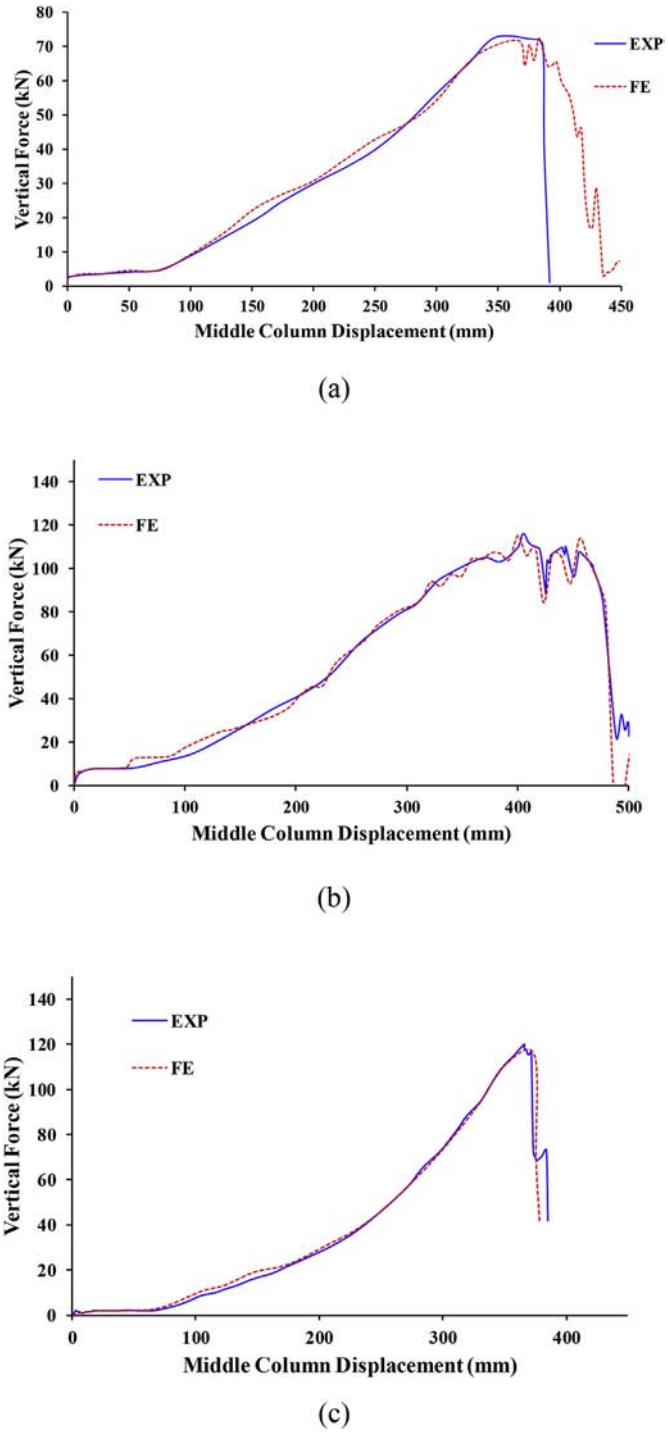

Fig. 16. Comparison of load vs displacement envelopes for: (a) Assembly S-P-B-2D of this study; (b) Assembly S-P-B-3D of this study; (c) Assembly S-W-C tested by Yang and Tan [40].

Fig. 15. Numerically predicted failure mode for: (a) Assembly S-P-B-2D of this study; (b) Assembly S-P-B-3D of this study; (c) Assembly S-W-C tested by Yang and Tan [40]; (d) Legend of Von Mises stress contours.

Table 5
FE analysis matrix for numerically studied shear beam-column connections.

Specimen ID	Type of shear connection	Connection with beam	Connection with column	Bolt/Welding	Type of frame assembly
S-P-W-2D	Single shear plate	Single shear plate welded to web of beam	Single shear plate welded to flange of column	Fillet Welded	2D assembly (see Fig. 17(a))
S-P-W-3D	Single shear plate	Single shear plate welded to web of beam	Single shear welded to flange and web of column	Fillet Welded	3D assembly (see Fig. 17(b))
D-A-B-2D	Double angle	Double angle bolted to web of beam	Double angle bolted to flange of column	Bearing Bolt	2D assembly (see Fig. 17(c))
D-A-B-3D	Double angle	Double angle bolted to web of beam	Double angle bolted to flange and web of column	Bearing Bolt	3D assembly (see Fig. 17(d))
D-A-W-2D	Double angle	Double angle welded to web of beam	Double angle welded to flange of column	Fillet Welded	2D assembly (see Fig. 17(e))
D-A-W-3D	Double angle	Double angle welded to web of beam	Double angle welded to flange and web of column	Fillet Welded	3D assembly (see Fig. 17(f))
D-A-B-W-2D	Double angle	Double angle bolted to web of beam	Double angle welded to flange of column	Bearing Bolt /Fillet Welded	2D assembly (see Fig. 17(g))
D-A-B-W-3D	Double angle	Double angle bolted to web of beam	Double angle welded to flange and web of column	Bearing Bolt /Fillet Welded	3D assembly (see Fig. 17(h))

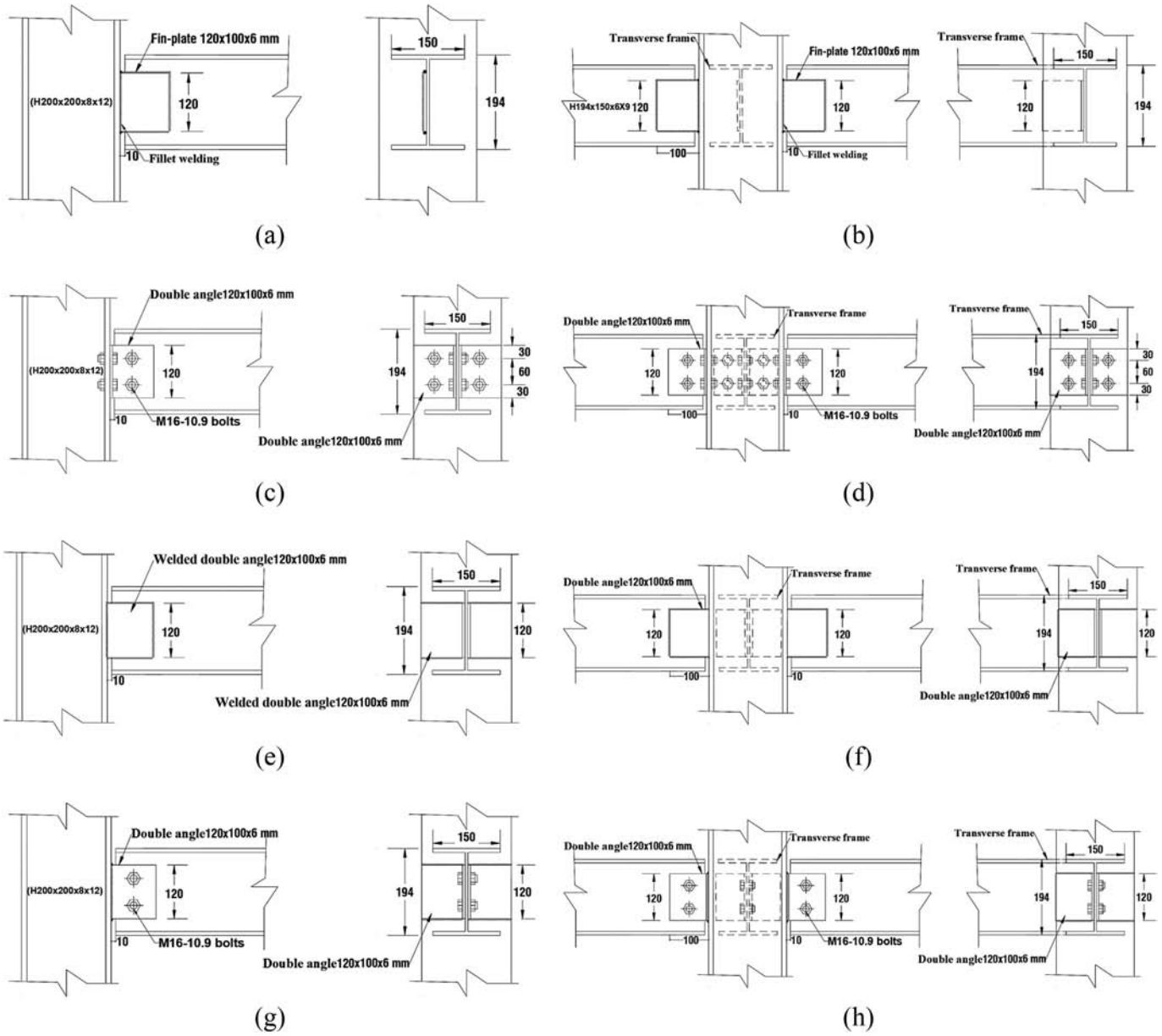

Fig. 17. Details of numerically investigated beam-column connections (Dimensions are measured in mm): (a) Assembly S-P-W-2D; (b) Assembly S-P-W-3D; (c) Assembly D-A-B-2D; (d) Assembly D-A-B-3D; (e) Assembly D-A-W-2D; (f) Assembly D-A-W-3D; (g) Assembly D-A-B-W-2D; (h) Assembly D-A-B-W-3D.

level, tensile axial force was initiated in the beam, which indicates the beginning of catenary action phase. As depicted from Table 6 and Fig. 21, the specimen reached its maximum load of catenary action phase (126 kN) at a displacement of 559 mm. At this displacement level, failure occurred in the middle connection because of fracture of angles owing to the significant tensile axial force in the beams (see Fig. 18(c)).

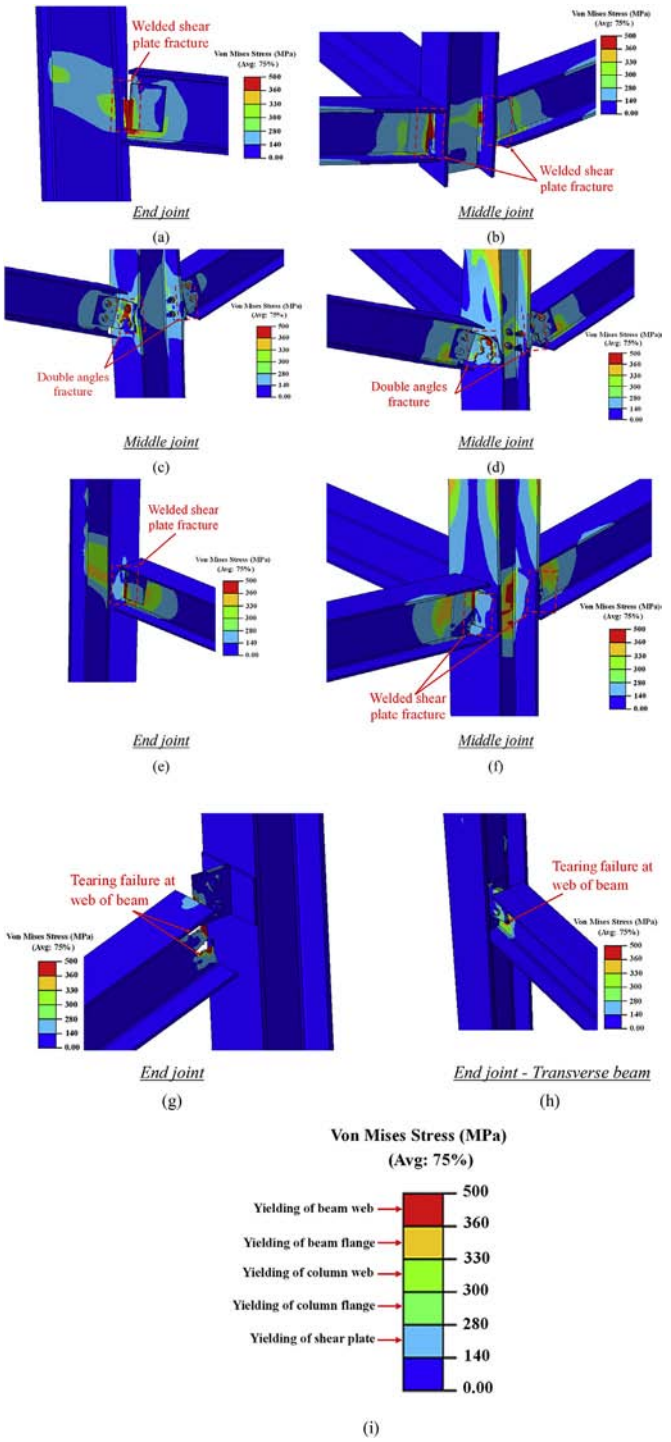

Fig. 18. FE failure mode for numerically investigated beam-column connections: (a) Assembly S-P-W-2D; (b) Assembly S-P-W-3D; (c) Assembly D-A-B-2D; (d) Assembly D-A-B-3D; (e) Assembly D-A-W-2D; (f) Assembly D-A-W-3D; (g) Assembly D-A-B-W-2D; (h) Assembly D-A-B-W-3D; (i) Legend of Von Mises stress contours.

Fig. 22 shows load versus displacement relationship for assembly D-A-B-3D. In the preliminary loading phase, the behavior of the specimen was nearly the same as specimen D-A-B-2D. It is noted that prior to its failure, specimen D-A-B-3D had larger rotation and displacement than the previous 3D simple specimens (S-P-B-3D and S-P-W-3D). Failure of specimen D-A-B-3D was at a middle column displacement of about 556 mm that is correspondent to a peak load of nearly 215 kN and a beam chord rotation of about 15.5°. This failure was due to fracture of angles at the middle connection. This fracture propagated through the angles until the specimen could not take additional loading, as seen in Fig. 18(d).

Load-displacement characteristics for assembly D-A-W-2D is presented in Fig. 23. During the preliminary loading stage, the behavior of the specimen was nearly in the linear elastic stage without obvious damage. Following the initial yielding of the welded double angle, the load-displacement response was nonlinear with reduction in the secant stiffness. As shown in Fig. 23 and Table 6, the specimen reached its maximum load of flexural action phase (67 kN) at a displacement of 75 mm. At this displacement level, tensile axial force was initiated in the beam, which indicates the beginning of catenary action phase. Maximum load of catenary action phase was 100 kN, as depicted from Fig. 23 and Table 6. The outer connection failed at displacement of 225 mm because of fracture of welded double angles owing to the significant tensile axial force in the beams (see Fig. 18(e)).

Fig. 24 presents load versus displacement characteristics for frame D-A-W-3D. In the preliminary loading stage, the behavior of the specimen was in the almost in the linear elastic stage without obvious damage. Following the initial yielding of the welded double angles, the load-displacement response was nonlinear with reduction in the secant stiffness. It is noted that prior to its failure, specimen D-A-W-3D had less displacement and rotation than specimen D-A-W-2D. At a middle column displacement of nearly 217 mm, failure of specimen D-A-W-3D occurred, which corresponded to maximum load of almost 132 kN and beam chord rotation of nearly 2.2°. Failure of specimen D-A-W-3D owed to fracture of the welded double angles at the middle beam-column connection. This fracture propagated through the plates until the specimen could not take additional loading (Fig. 18(f)).

Fig. 25 presents load-displacement response for frame D-A-B-W-2D and its numerically predicted failure mode is shown in Fig. 18(g). Compared with the former joints, the bolted double angle to web of beam and welded to flange of column connection (D-A-B-W-2D) has a lower rotation capacity than the fully bolted joint D-A-B-2D and larger rotation capacity than the fully welded connection D-A-W-2D. Failure of connection D-A-B-W-2D was due to tearing at web of beam (see Fig. 18(g)), which was at a maximum load of 74 kN (the corresponding center column displacement was 322 mm as seen in Fig. 25). Failure was also characterized by significant bearing deformation of the bolted angles around the holes of the bolts. This specimen could resist small load at small displacement levels until the formation of different actions at large values of center column displacement. It should be noted that specimen D-A-B-W-2D has limited load capacity due to the small rotation limit of the joint compared with the rest 2D double angle (bolted and welded) web-cleats connections.

For specimen D-A-B-W-3D which is similar to D-A-B-W-2D but with adding a transverse beam at the middle joint, there is no distinct flexural phase as depicted from the load-displacement curve in Fig. 26. The small deformation of the beam web close to the exterior column revealed the onset of yielding after which the second phase was initiated with

Table 6
Key elements of load-displacement response for numerically studied shear beam-column connections[a]

Specimen ID	Flexural action stage				Catenary action stage				P_u (kN)	Δ_u (mm)	E_u (kN.m)	θ (degree)	Mode of failure
	P_y (kN)	Δ_y (mm)	$P_{u,FA}$ (kN)	$\Delta_{u,c\text{-}FA}$ (mm)	$P_{u,CA}$ (kN)	$P_{u,CA}$ / $P_{u,FA}$	$\Delta_{u,c\text{-}CA}$ (mm)	$N_{u,CA}$ (kN)					
Fin-plate connections													
S-P-W-2D	18	6	47	102	81	1.72	194	263	81	225	11.4	5.5	Fracture of shear plate
S-P-W-3D	38	6	84	78	151	1.8	257	270	151	257	36.5	7.3	Fracture of shear plate
Double angle (bolted and welded) web-cleat connections													
D-A-B-2D	–	–	9	102	126	14	559	197	126	597	27.1	15.6	Fracture of angles
D-A-B-3D	–	–	6	102	215	34.2	556	226	215	646	52.5	15.5	Fracture of angles
D-A-W-2D	24	6	67	75	100	1.5	150	408	100	234	17.3	4.3	Fracture of angles
D-A-W-3D	33	6	87	75	132	1.5	149	427	132	217	21	2.2	Fracture of angles
D-A-B-W-2D	–	6	15	70	74	5	322	213	74	497	15.2	9.2	Tearing failure at web of beam
D-A-B-W-3D	–	6	18	74	117	6	330	218	117	486	24	9.4	Tearing failure at web of transverse beam

[a] P_y load at first yield of plate or angle at inner column face; Δ_y = displacement of middle column at first yield of beam bottom flange at inner column face; $P_{u,FA}$ = peak load of flexural action stage; $\Delta_{u,c\text{-}FA}$ = displacement of middle column at peak load of flexural action stage; $P_{u,CA}$ = peak load of catenary action stage; $\Delta_{u,c\text{-}CA}$ = displacement of middle column at peak load of catenary action stage; $N_{u,CA}$ = peak beam axial force at catenary action stage; P_u = progressive collapse resistance; Δ_u = displacement of middle column at ultimate state; E_u = energy dissipated at ultimate state; and θ = beam rotation at maximum load.

reduction in the flexural stiffness. The specimen reached its maximum load of flexural action phase (18 kN) at a displacement of 74 mm. Nevertheless, as seen in Fig. 26 and Table 6, maximum load of catenary action phase was about 117 kN that is correspondent to a center column displacement of 330 mm. As depicted from Fig. 18(h), the transverse beam at outer joint fractured by tearing failure at its web.

6. Comparison of simple connections

It is explicable from Table 6 that for investigated simple beam-column joints, the progressive collapse resistance for specimens with simple bolted connections could increase significantly under a middle column removal scenario if tensile axial force (catenary action) is taken into account in beams. However, frame assemblies with simple welded joints could attain their maximum load without the effect of catenary action.

Fig. 27 illustrates comparison of load-displacement curves for all studied connections. As confirmed from the results of both experimental and numerical study, the investigated steel beam-column joints experienced three distinct performance phases (elastic phase, flexural action phase and catenary action phase). At low displacement levels, only simple welded connection specimens stayed firstly in the elastic phase. In this phase, assemblies S-P-W-3D and D-A-W-3D have the highest load resistance. Once the tab plate and angles at middle connection have yielded, the second phase of behavior was initiated and the specimens carried loads through flexural action phase. In this phase, frame D-A-W-3D attained the highest load capacity followed, respectively, by frames S-P-W-3D, D-A-W-2D, and S-P-W-2D as shown in Fig. 27 and Table 6. For the remaining frames, their behavior is nearly similar to frame S-P-B-2D. Tensile axial forces were developed in the beams with the increase in the center column displacement, signifying the formation of catenary action phase. In this phase, specimens D-A-W-3D, D-A-W-2D, S-P-W-3D and S-P-W-2D performed well. For instance, for frame D-A-W-3D, it is revealed from Fig. 27 that the tensile axial force increased in the beam until the joint was not able to carry any additional stresses resulting from combined bending moment and axial force.

Performance of studied simple shear steel beam-column connections was compared in terms of their resistance to progressive collapse risk. Accordingly, connections of 3D assemblies were ranked in the order of increasing level of performance (peak load and dissipated energy) as seen in Figs. 28(a) and (b) for peak load and dissipated energy, respectively. It is found that among all studied connections, the double angle bolted web-cleats connection (specimen D-A-B-3D) had the largest resistance to progressive collapse risk in terms of peak load and dissipated energy. This connection was followed by the welded shear plate connection (specimen S-P-W-3D). It was also identified from Fig. 28 that the lowest peak load was given by the bolted shear plate connection (specimen 3D-S-1); however, the minimum dissipated energy was provided by the double angle welded web-cleats connection (specimen D-A-W-3D).

Figs. 9, 15, and 18 compare between the modes of failure of the 2D and 3D assemblies. It is generally identified that at higher levels of middle column displacement, concentration of stresses around the middle connection of the 2D assembly was noticeably lower than that in the 3D assemblies, especially in the welded connections. This could be attributed to the higher axial tension developed in the beams of the 3D assembly during the final stages of loading. The effect of transverse beam on the progressive collapse resistance of different simple beam-column connections is illustrated in Figs. 29(a) and (b) with regard to percent increase in peak load and dissipated energy, respectively. It is clear that both strength and ductility of the assembly were significantly increased owing to the effect of transverse beam. The 2D assemblies gave lower bound solution for the progressive collapse resistance, and the better performance of the 3D assemblies is expected. This is because in the 3D assemblies, the load applied on the middle column is resisted by three beams and the energy input in the assembly is dissipated in six connections; whereas, in the 2D assemblies, the load is shared by two beams and the energy is dissipated into four connections. As seen in Fig. 29(a), the transverse beam enhanced the peak load of the assembly by about 32% to 86% (average = 61%). However, the increase in the dissipated energy due to effect of transverse beam ranged from 21% to 220% (average = 104%), as shown in Fig. 29(b).

The beneficial effect of the 3D response is the major load mobility mechanism following the removal of primary load-bearing element in multistory buildings. Such beneficial effect is often ignored while studying progressive collapse through 2D substructures. Consequently, the progressive collapse resistance of steel framed buildings is often underestimated when testing 2D beam-column assemblies under the event of middle column removal. Efforts should be made to study the progressive collapse by investigating the full steel framed building or

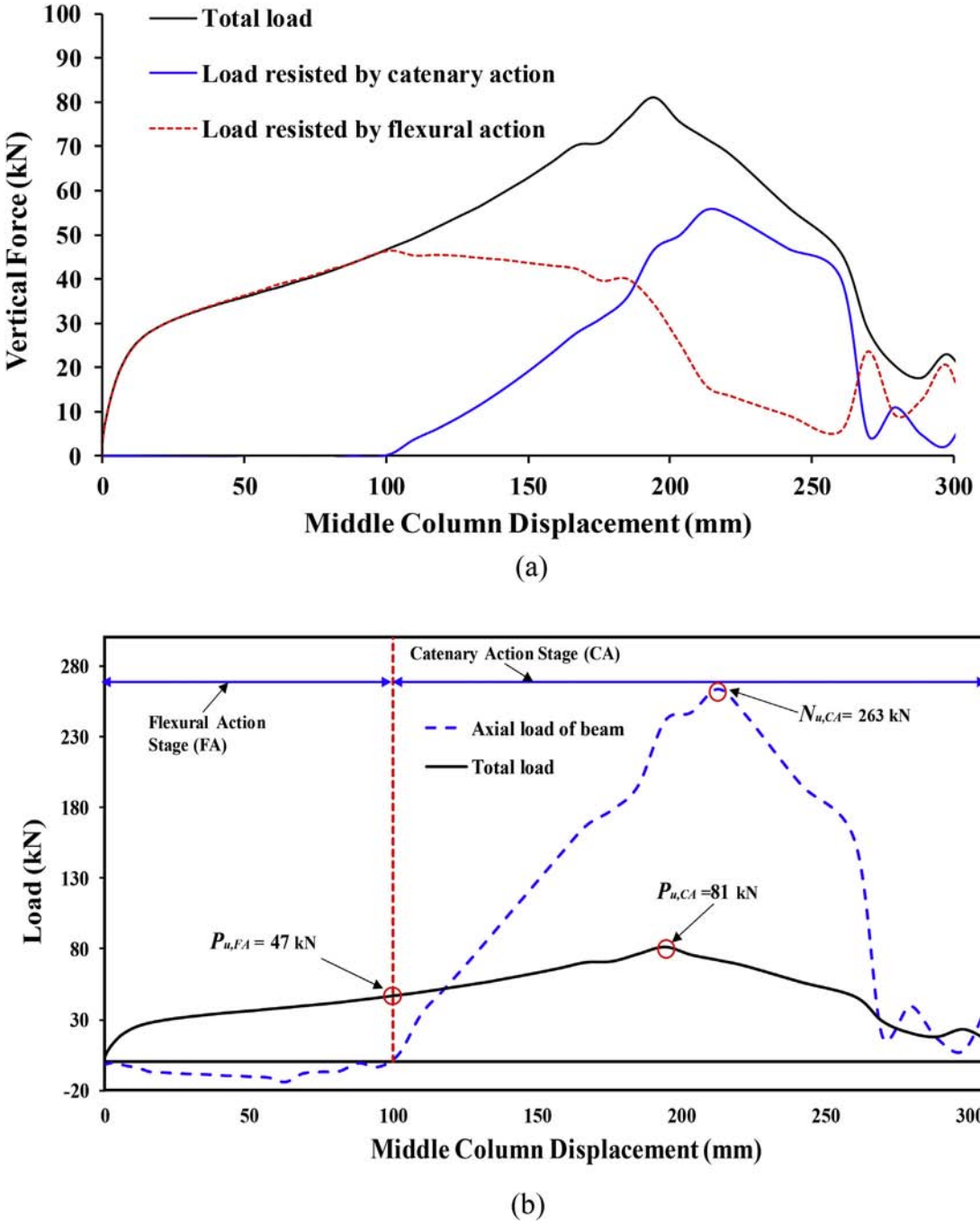

Fig. 19. Load vs displacement relationship for assembly S-P-W-2D: (a) Envelope of load vs displacement; (b) Flexural and catenary action phases.

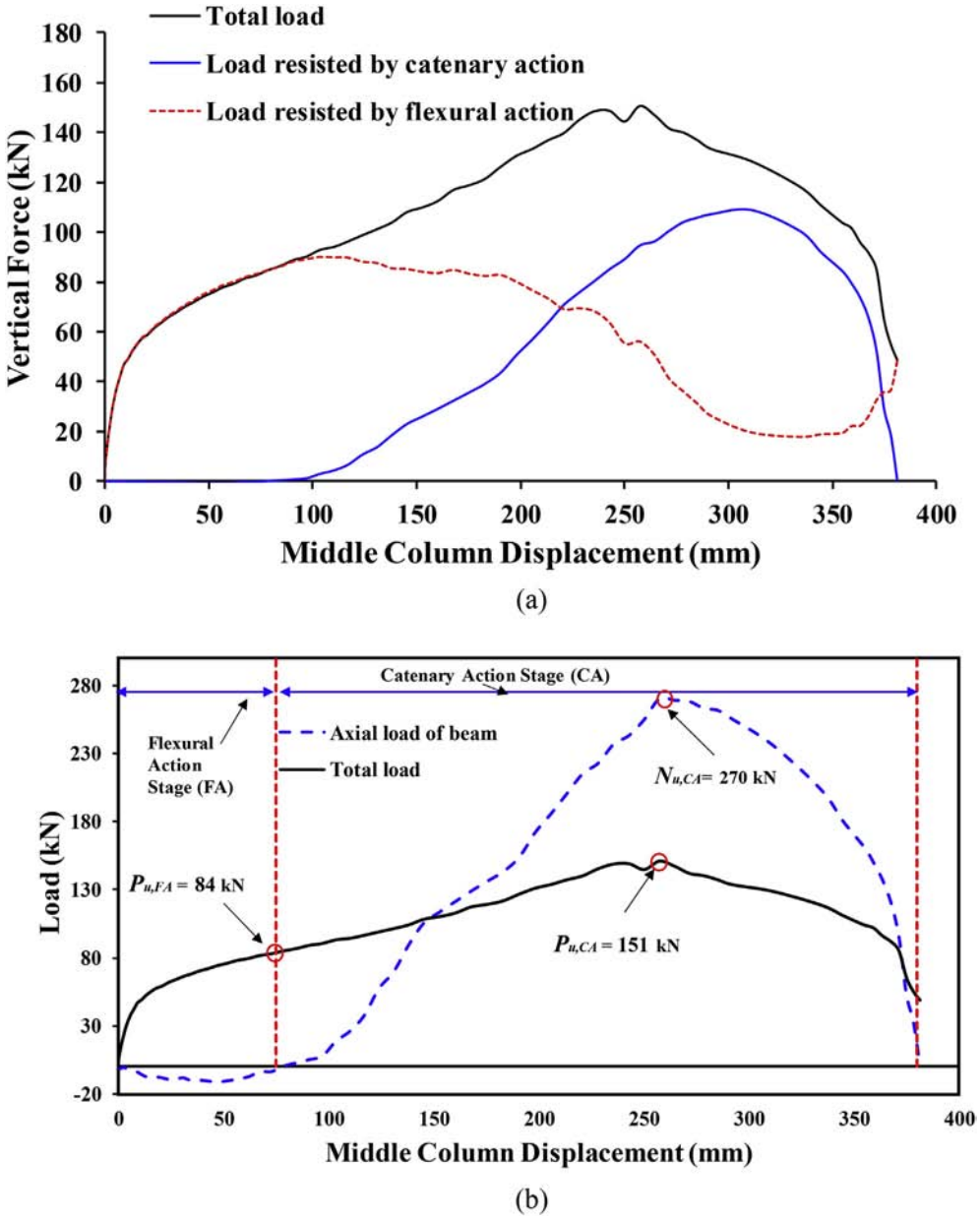

Fig. 20. Load vs displacement relationship for assembly S-P-W-3D: (a) Envelope of load vs displacement; (b) Flexural and catenary action phases.

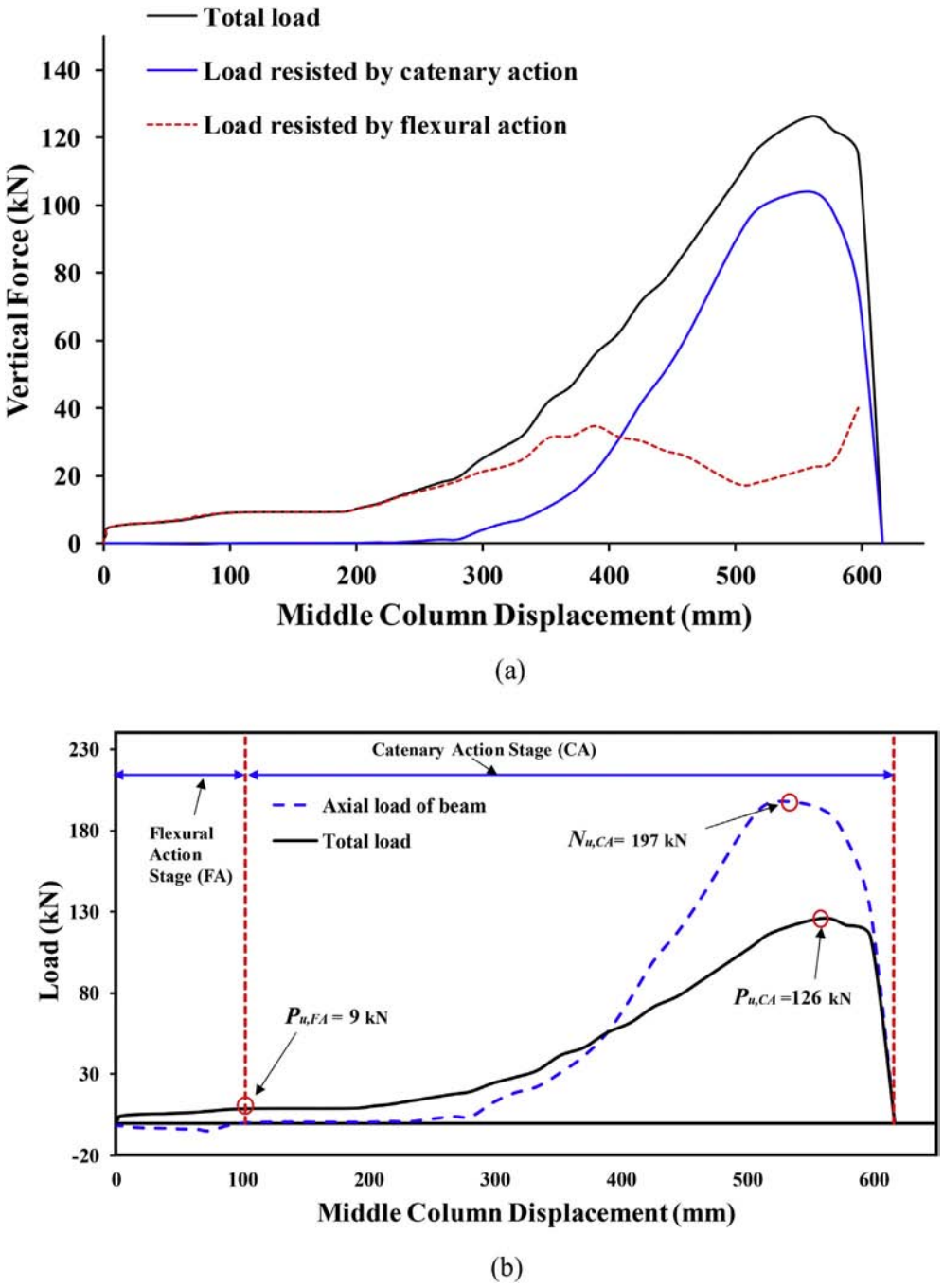

Fig. 21. Load vs displacement relationship for assembly D-A-B-2D: (a) Envelope of load vs displacement; (b) Flexural and catenary action phases.

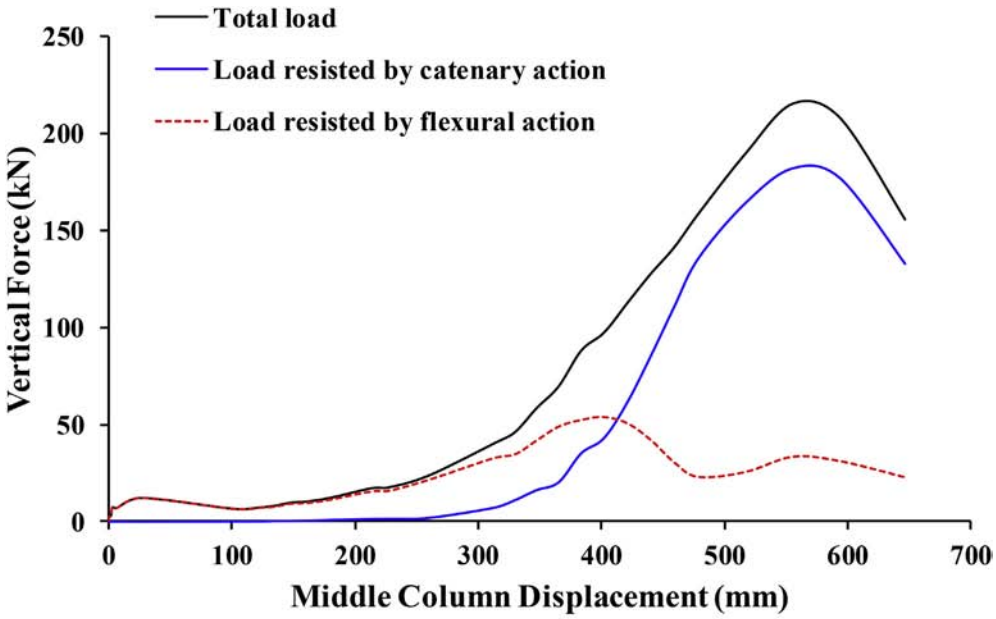

(a)

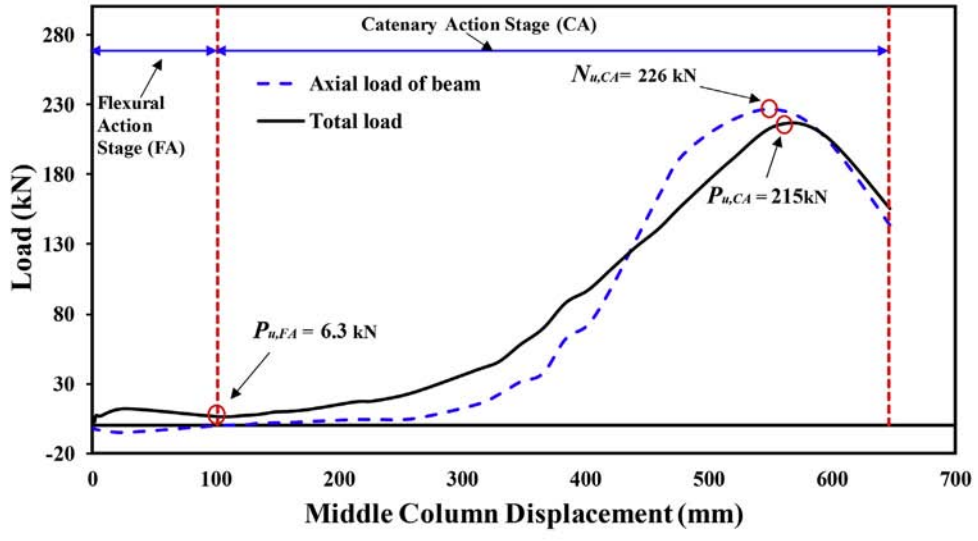

(b)

Fig. 22. Load vs displacement relationship for assembly D-A-B-3D: (a) Envelope of load vs displacement; (b) Flexural and catenary action phases.

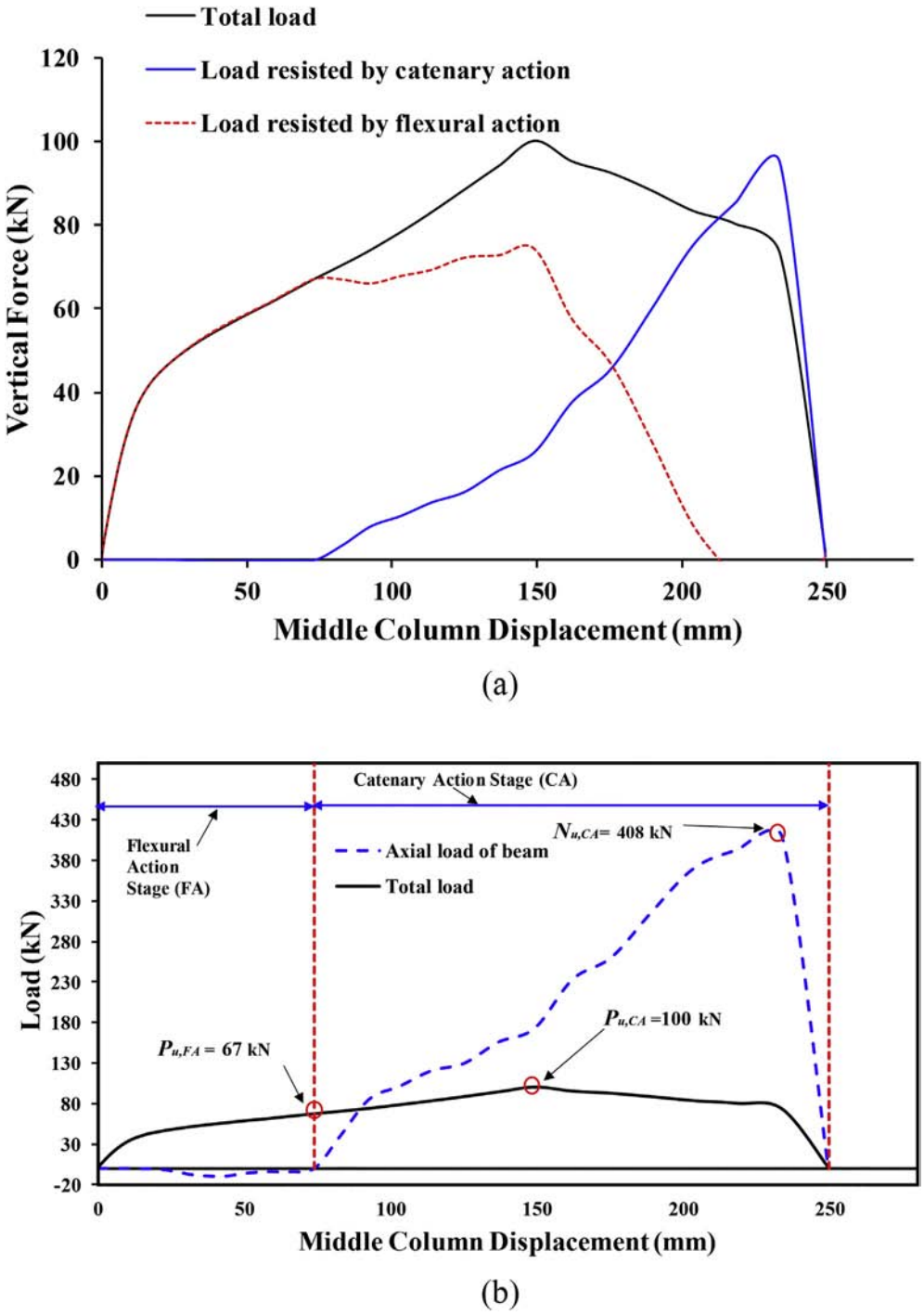

Fig. 23. Load vs displacement relationship for assembly D-A-W-2D: (a) Envelope of load vs displacement; (b) Flexural and catenary action phases.

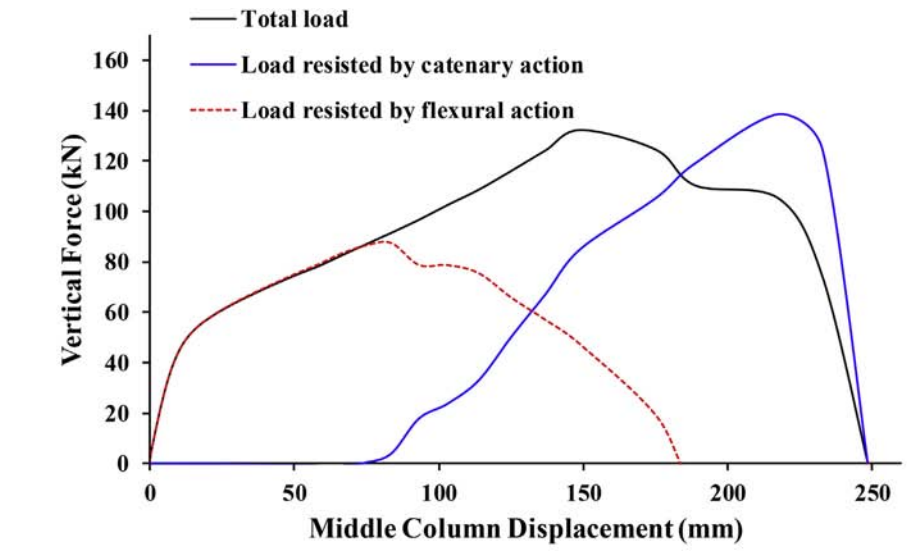

(a)

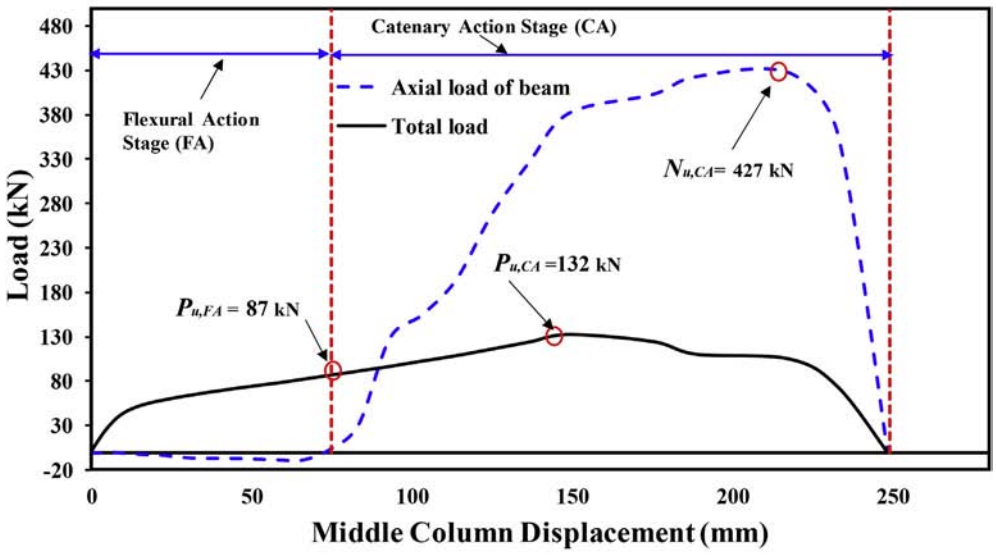

(b)

Fig. 24. Load vs displacement relationship for assembly D-A-W-3D: (a) Envelope of load vs displacement; (b) Flexural and catenary action phases.

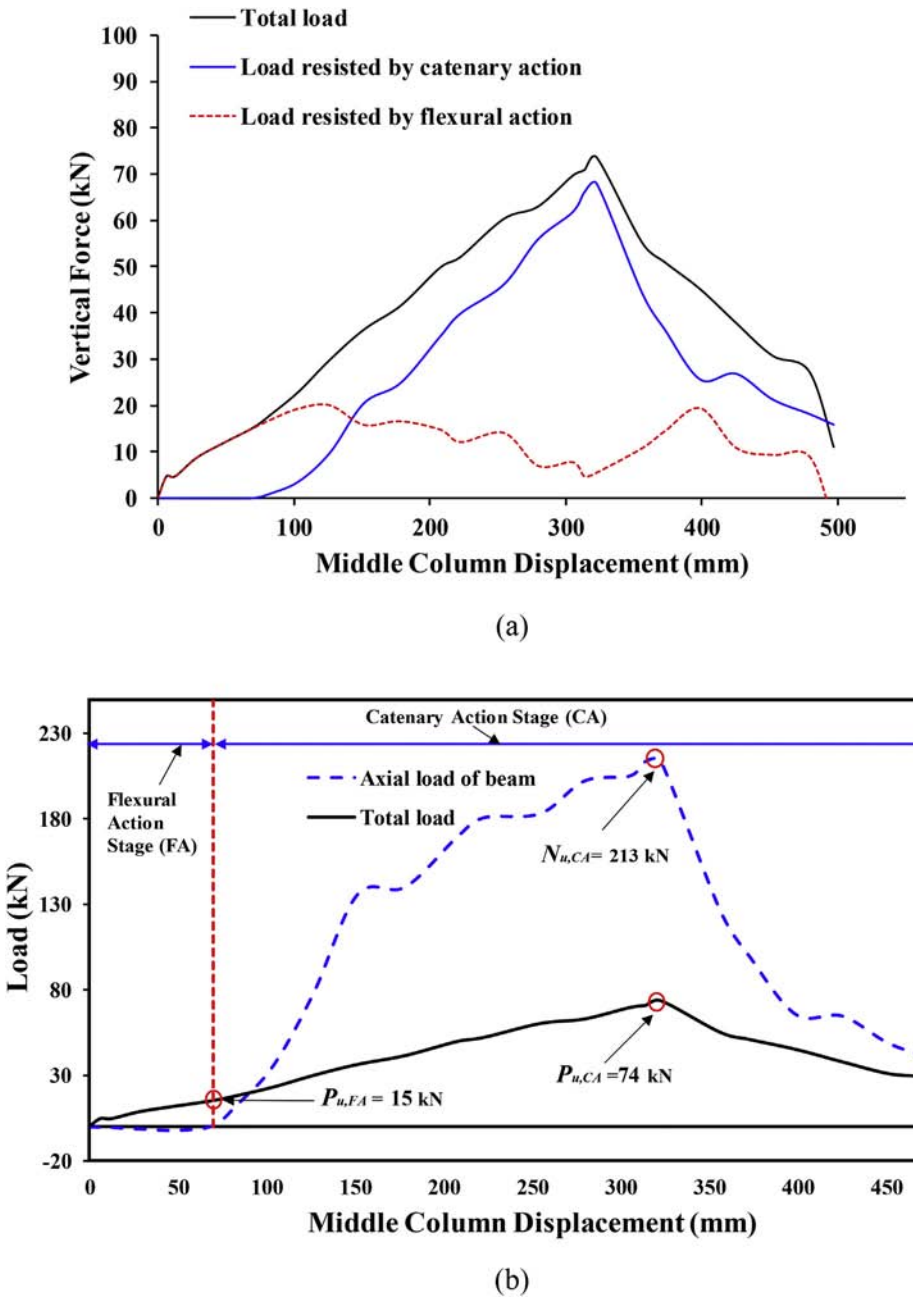

Fig. 25. Load vs displacement relationship for assembly D-A-B-W-2D: (a) Envelope of load vs displacement; (b) Flexural and catenary action phases.

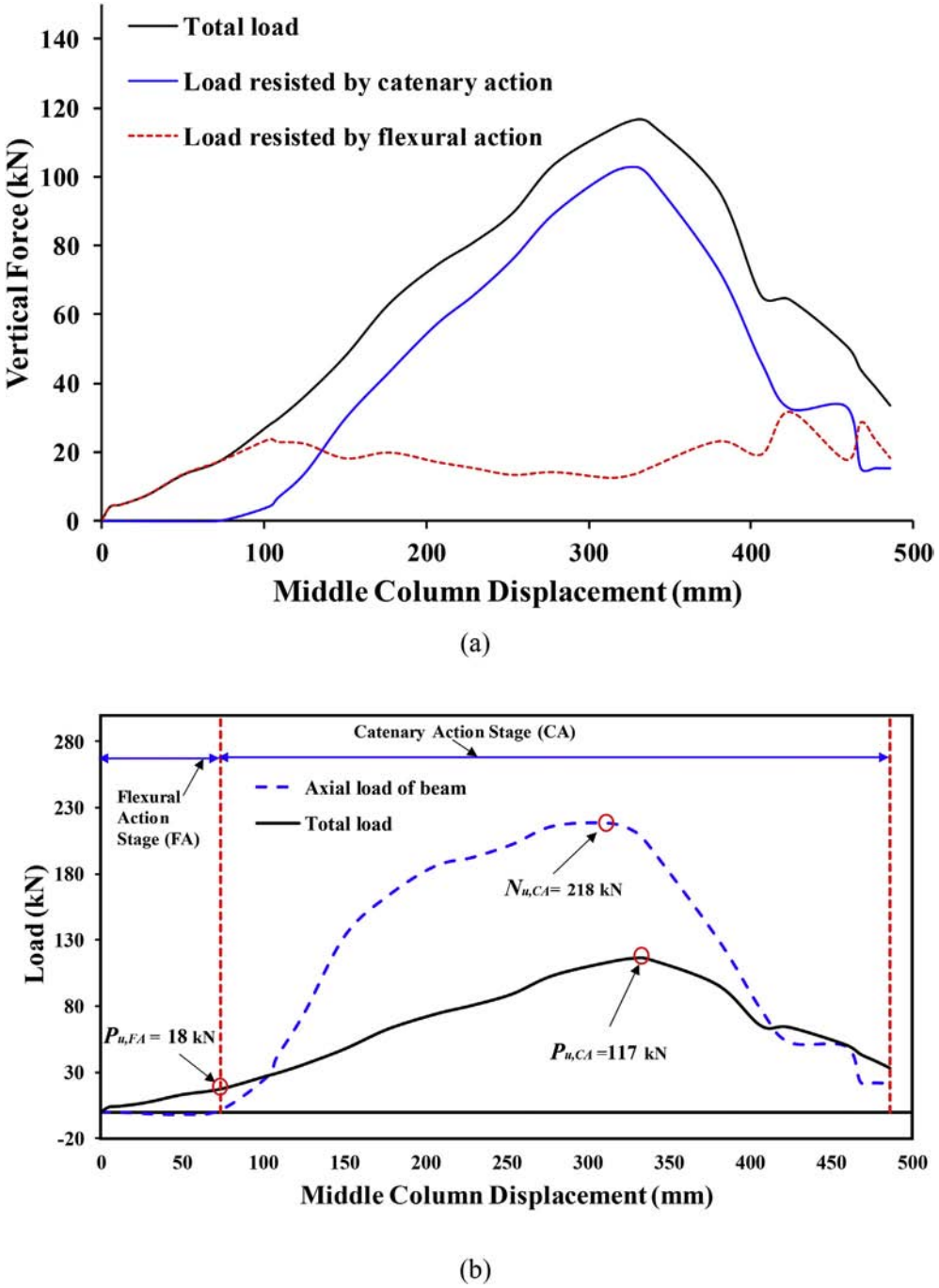

Fig. 26. Load vs displacement relationship for assembly D-A-B-W-3D: (a) Envelope of load vs displacement; (b) Flexural and catenary action phases.

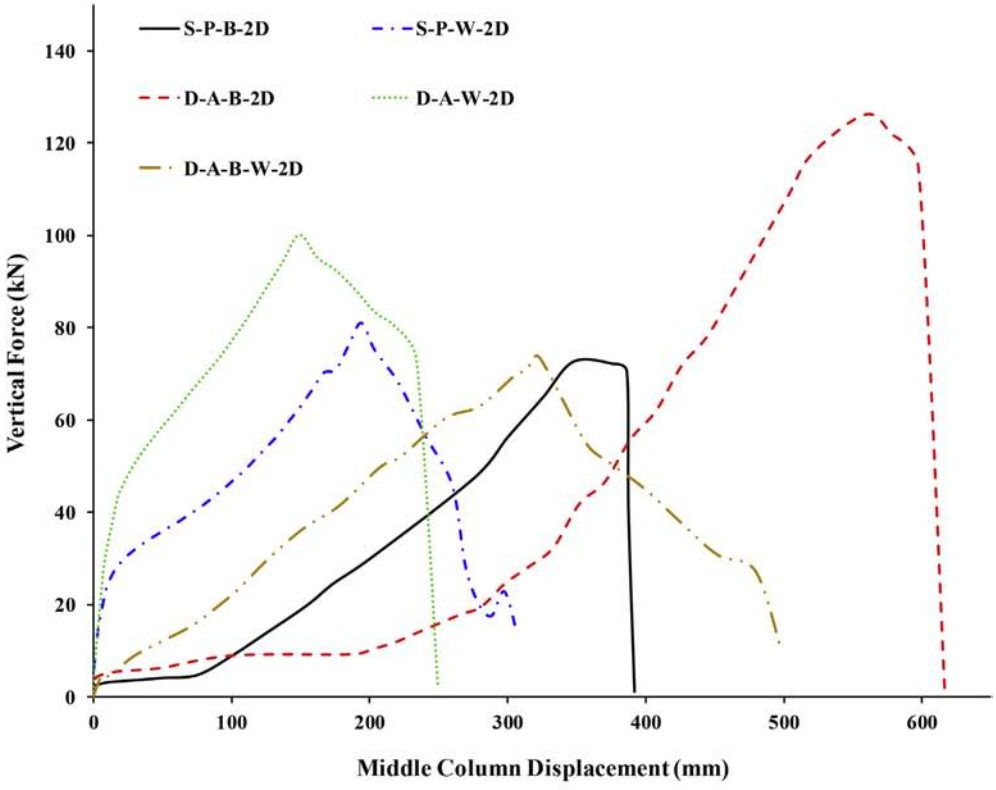

(a)

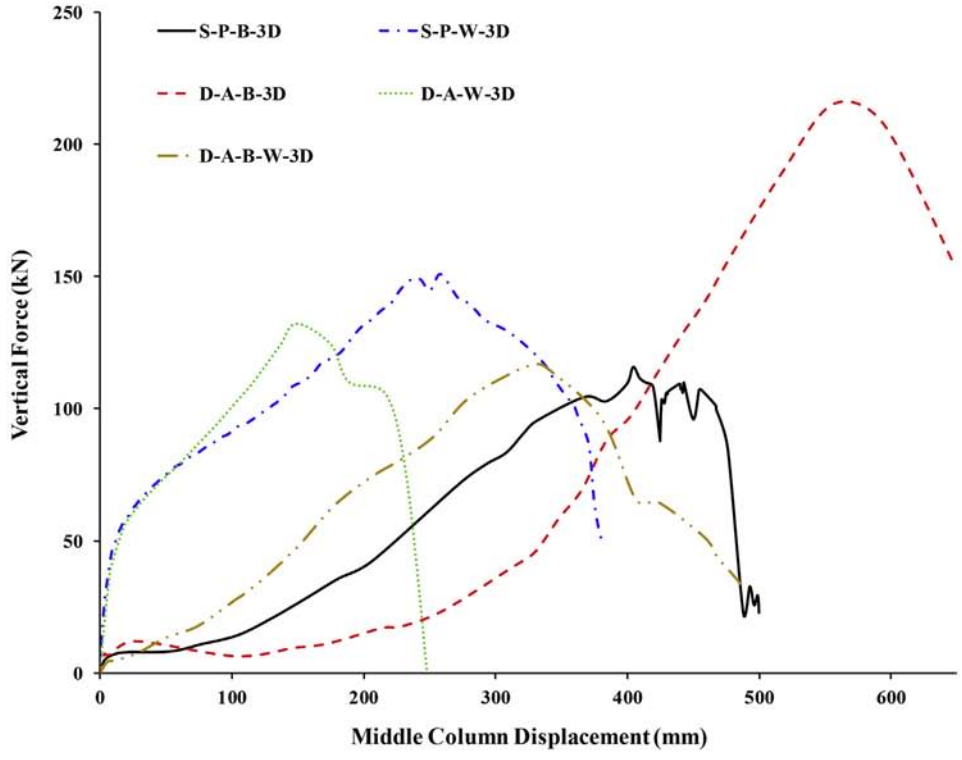

(b)

Fig. 27. Load-displacement comparison for: (a) 2D assemblies; (b) 3D assemblies.

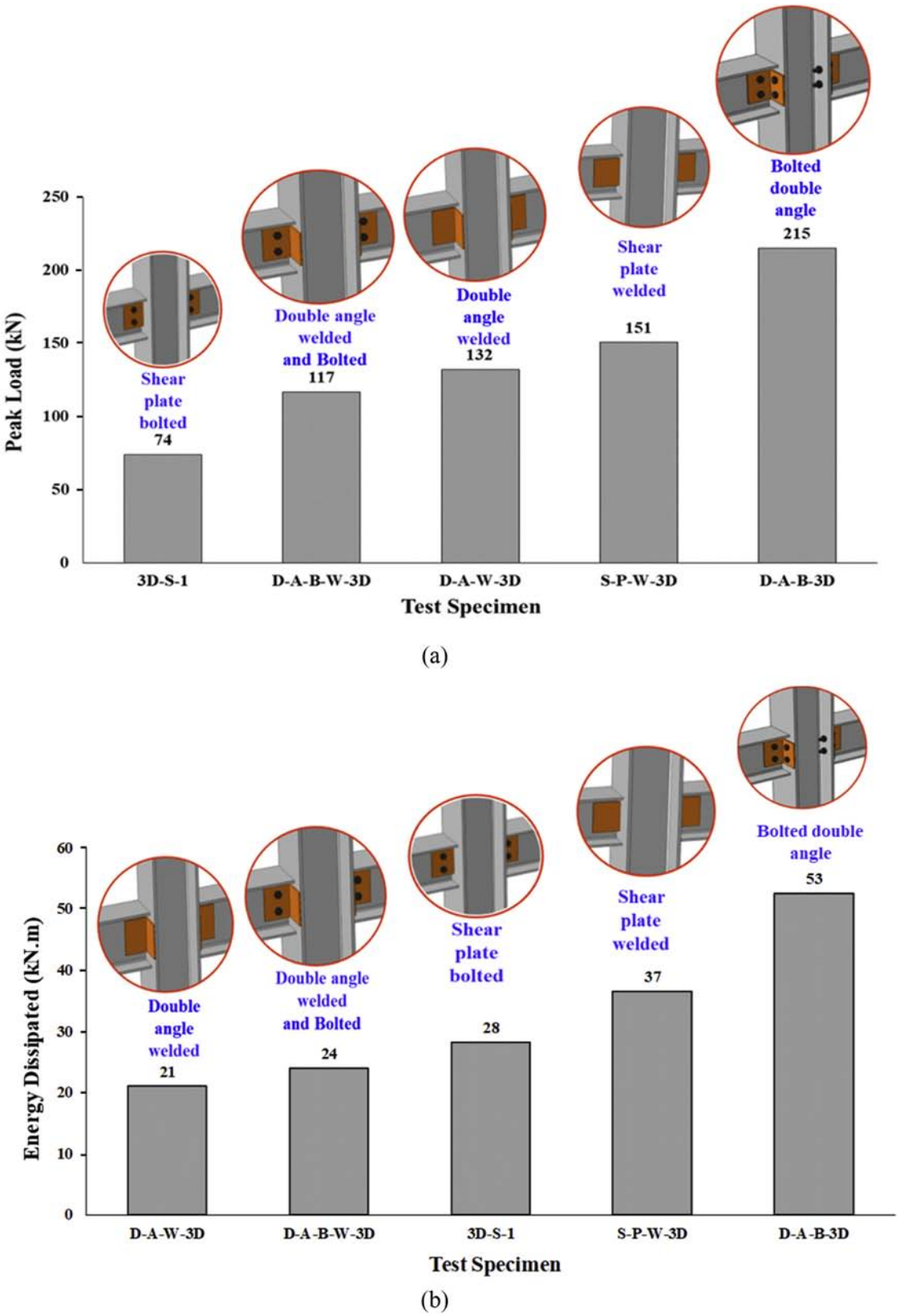

Fig. 28. Comparison of studied simple beam-column connections with regard to: (a) Peak load for 3D assembly; (b) Energy dissipated at ultimate state for 3D assembly.

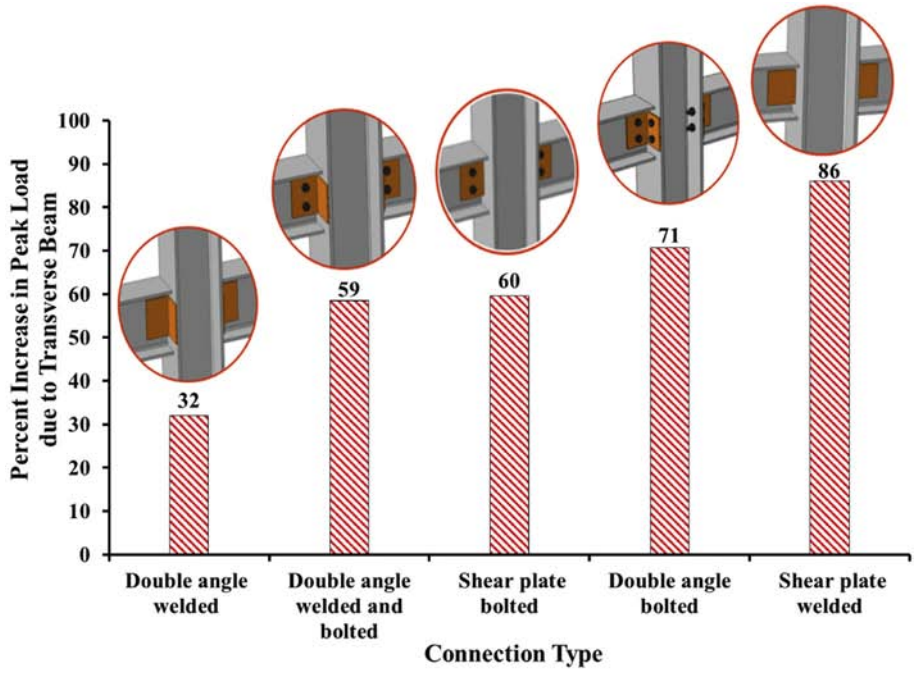

(a)

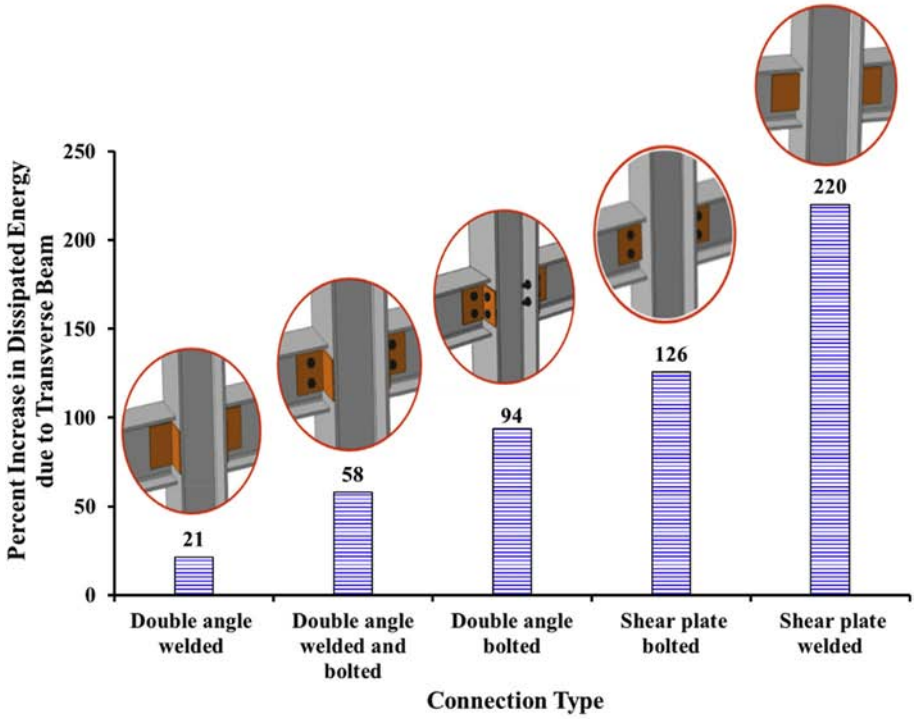

(b)

Fig. 29. Effect of transverse beam on progressive collapse risk with respect to: (a) Peak load; (b) Energy dissipated at ultimate state.

at least testing 3D assemblies so that the realistic progressive collapse resistance can be captured.

7. Conclusions

The key conclusions of current study can be itemized as follows:

1. Steel frame assemblies with investigated types of simple beam-column connections had a limited progressive collapse resistance. This resulted from the discontinuity of the beams across the joint zone. Therefore, the beams were incapable of redistributing the load taken by failed column to nearby steel elements.
2. For the 3D assembly with bolted shear plate connection studied experimentally in current study (specimen S-P-B-3D), large catenary action was not mobilized and the beam axial force was considerably small due to fracture of shear plate connecting transverse beam with middle column. However, for the same 3D assembly with double angle bolted web-cleats connections (specimen D-A-B-3D), significant axial tensile forces were generated in the beams and the catenary action stage was then more distinct, providing an increase in the progressive collapse resistance by about 85% more than that for specimen S-P-B-3D. This reveals the significance of the type of connector (double angle) between beam and column flanges on the progressive collapse resistance of beam-column joints subjected to column-loss events.
3. For simple shear joints studied in this research, if axial force in beams (catenary behavior) is accounted for under a middle column-missing event, the progressive collapse resistance could increase considerably for frame assemblies with bolted connections. However, assemblies with welded joints could reach their peak load resistance without the influence of catenary action.
4. The transverse beam has led to major improvement in the progressive collapse resistance of the 3D beam-column assemblies in comparison with the 2D assemblies. The average enhancements due to the effect of transverse beam were 61% and 104% for peak load and dissipated energy, respectively. Consequently, the progressive collapse resistance of steel framed buildings is often underestimated when testing 2D beam-column assemblies under the event of middle column removal. Efforts should be made to study the progressive collapse by investigating the full steel framed building or at least testing 3D assemblies so that the realistic progressive collapse resistance can be captured.
5. For the 2D and 3D assemblies with both welded and bolted double angle connections (specimens D-A-B-W-2D and D-A-B-W-3D), even though the failure modes are due to tearing failure at web of beam, failure was noted to be ductile with enhanced energy dissipation. Before occurrence of failure, tab plate of the exterior joint has yielded, which resulted in the development of large axial tensile force in the beams. This in turn mobilized the catenary action stage.
6. Performance of studied simple shear steel beam-column connections was compared in terms of their resistance to progressive collapse risk. Among all studied connections, the double angle bolted web-cleats connection (specimen D-A-B-3D) had the largest resistance to progressive collapse risk in terms of peak load and dissipated energy. This connection was followed by the welded shear plate connection (specimen S-P-W-3D). These two types are thus recommended for design codes of practice to be used as simple shear beam-column connections in multistory steel framed buildings in order to minimize the progressive collapse risk and then save human lives. The lowest peak load was given by the bolted shear plate connection (specimen 3D-S-1). Therefore, this connection should be avoided, wherever possible, in multistory steel framed buildings.

Declaration of Competing Interest

The authors declare that there is no conflict of interest regarding the publication of this article.

Acknowledgement

The authors are grateful to the Deanship of Scientific Research, King Saud University, for funding through Vice Deanship of Scientific Research Chairs.

References

[1] W. McGuire, Prevention of progressive collapse, Proc. Regional Conf. on Tall Buildings, 1974 , Bangkok, Thailand.
[2] E.V. Leyendecker, B.R. Ellingwood, Design Methods for Reducing the Risk of Progressive Collapse in Buildings, National Bureau of Standards, Washington, DC, 1977.
[3] W.G. Corley, P.F. Mlakar, M.A. Sozen, C.H. Thornton, The Oklahoma City bombing: summary and recommendations for multihazard mitigation, J. Perform. Constr. Facil. 12 (3) (1998) 100–112.
[4] Z.P. Bazant, Y. Zhou, Why did the world trade center collapse?-simple analysis, J. Eng. Mech. 128 (1) (2002) 2–6.
[5] Z.P. Bazant, M. Verdure, Mechanics of progressive collapse: learning from world trade center and building demolitions, J. Eng. Mech. 133 (3) (2007) 308–319.
[6] Z.P. Bazant, J. Le, F.R. Greening, D.B. Benson, What did and did not cause collapse of world trade center twin towers in New York, J. Eng. Mech. 134 (10) (2008) 892–906.
[7] K.A. Seffen, Progressive collapse of the world trade center: simple analysis, J. Eng. Mech. 134 (2) (2008) 125–132.
[8] K. Khandelwal, S. El-Tawil, F. Sadek, Progressive collapse analysis of seismically designed steel braced frames, J Const Steel Res 65 (2009) 699–708.
[9] J. Kim, T. Kim, Assessment of progressive collapse-resisting capacity of steel moment frames, J Const Steel Res 65 (2009) 169–179.
[10] J. Kim, D. An, Evaluation of progressive collapse potential of steel moment frames considering catenary action, Struct Des Tall Spec 18 (2009) 455–465.
[11] D. Grierson, M. Safi, L. Xu, Y. Liu, Simplified methods for progressive-collapse analysis of buildings. Proc. Metropolis and Beyond, Structures Congress, Reston, VA (2005) https://doi.org/10.1061/40753(171)225.
[12] B.A. Izzuddin, A.G. Vlassis, A.Y. Elghazouli, D.A. Nethercot, Progressive collapse of multistory buildings due to sudden column loss. Part I: simplified assessment framework, Eng. Struct. 30 (2008) 1308–1318.
[13] A.G. Vlassis, B.A. Izzuddin, A.Y. Elghazouli, D.A. Nethercot, Progressive collapse of multistorey buildings due to sudden column loss—part II: application, Eng. Struct. 30 (2008) 1424–1438.
[14] C. Lee, S. Kim, K. Han, K. Lee, Simplified nonlinear progressive collapse analysis of welded steel moment frames, J Const Steel Res 65 (2009) 1130–1137.
[15] A. Naji, F. Irani, Progressive collapse analysis of steel frames: Simplified procedure and explicit expression for dynamic increase factor, Int J Steel Struct 12 (4) (2012) 537–549.
[16] H.M. Elsanadedy, T.H. Almusallam, Y.R. Alharbi, Y.A. Al-Salloum, H. Abbas, Progressive collapse potential of a typical steel building due to blast attacks, J. Constr. Steel Res. 101 (2014) 143–157.
[17] Livermore Software Technology Corporation (LSTC), LS-DYNA user's keyword manual (nonlinear dynamic analysis of structures in three dimensions) Volume 1. Version 971, LSTC, 2007 Livermore, California.
[18] A. Hadidi, R. Jasour, A. Rafiee, On the progressive collapse resistant optimal seismic design of steel frames, Struct. Eng. Mech. 60 (5) (2016) 761–779.
[19] ANSI/AISC 360–05. Specifications for structural steel buildings. American Institute of Steel Construction, Chicago, IL, USA; 2005.
[20] US Department of Defense (DoD), Unified facilities criteria (UFC), DoD minimum antiterrorism standards for buildings. Washington, DC, Department of Defense, UFC 4–010-01, US Army Corps of Engineering, 2002 31.
[21] M. Mirtaheri, M.A. Zoghi, Design guides to resist progressive collapse for steel structures, Steel Comp Struct 20 (2) (2016) 357–378.
[22] M.A. Zoghi, M. Mirtaheri, Progressive collapse analysis of steel building considering effects of infill panels, Struct. Eng. Mech. 59 (1) (2016) 59–82.
[23] C.H. Chen, Y.F. Zhu, Y. Yao, Y. Huang, Progressive collapse analysis of steel frame structure based on the energy principle, Steel Comp Struct 21 (3) (2016) 553–571.
[24] H. Abbas, N. Jones, Influence of strain hardening on bending moment–axial force interaction, Int. J. Mech. Sci. 55 (1) (2012) 65–77.
[25] M. Hosseini, H. Abbas, Strain hardening in M–P interaction for metallic beam of I-section, Thin-Walled Struct. 62 (2013) 243–256.
[26] S.W. Bae, R.A. LaBoube, A. Belarbi, A. Ayoub, Progressive collapse of cold-formed steel framed structures, Thin-Walled Struct. 46 (7–9) (2008) 706–719.
[27] Q. Han, X. Li, M. Liu, B.F. Spencer Jr., Performance analysis and macromodel simulation of steel frame structures with beam-column joints using cast steel stiffeners for progressive collapse prevention, Thin-Walled Struct 140 (2019) 404–415.
[28] S. Gerasimidis, Analytical assessment of steel frames progressive collapse vulnerability to corner column loss, J. Constr. Steel Res. 95 (2014) 1–9.
[29] Y. Alashker, S. El-Tawil, F. Sadek, Progressive collapse resistance of steel-concrete composite floors, Eng. Struct. 136 (10) (2010) 1187–1196.
[30] F. Sadek, S. El-Tawil, H.S. Lew, Robustness of composite floor systems with shear connections: Modeling, simulation and Evaluation, Eng Struct 134 (11) (2008) 1717–1725.
[31] S.B. Kang, K.H. Tan, H.Y. Liu, X.H. Zhou, B. Yang, Effect of boundary conditions on the behaviour of composite frames against progressive collapse, J. Constr. Steel Res. 138 (2017) 150–167.

[32] F. Dinu, I. Marginean, D. Dubina, I. Petran, Experimental testing and numerical analysis of 3D steel frame system under column loss, Eng. Struct. 113 (15) (2016) 59–70.
[33] H. Qiao, Y. Yang, J. Zhang, Progressive collapse analysis of multistory moment frames with varying mechanisms, J Perform Constr Facil 32 (4) (2018) 04018043.
[34] A. Naji, Progressive collapse analysis of steel moment frames: an energy-based method and explicit expressions for capacity curves, J Perform Constr Facil 33 (2) (2019) 04019008.
[35] A.H. Ebrahimi, M.E. Jamkhaneh, M.S. Amiri, 3D finite-element analysis of steel moment frames including long-span entrance by strengthening steel cables and diagonal concentrically braced frames under progressive collapse, Pract Period Struct Des Constr 23 (4) (2018) 04018025.
[36] C.M. Foley, K. Martin, C. Schneeman, Robustness in structural steel framing systems. Milwaukee, WI: Marquette University (2007 Jan 19).
[37] P. Pantidis, S. Gerasimidis, Progressive collapse of 3D steel composite buildings under interior gravity column loss, J. Constr. Steel Res. 150 (2018) 60–75.
[38] M. Alrubaidi, H. Elsanadedy, H. Abbas, T. Almusallam, Y. Al-Salloum, Investigation of different steel intermediate moment frame connections under column-loss scenario, Thin-Walled Struct 154 (2020) 106875.
[39] TEC-2007, Specification for buildings to be built in disaster areas, Ministry of Public Works and Settlement, Ankara, Turkey (2007).
[40] B. Yang, K.H. Tan, Experimental tests of different types of bolted steel beam–column joints under a central-column-removal scenario, Eng. Struct. 54 (2013) 112–130.
[41] Abaqus 6.17 Analysis User"s Guide, Section 12.9.3 – Defining Damages, Dassault Systemes Simulia Corp, Providence, RI, 2017.
[42] ANSI/AISC 360-16, Specifications for Structural Steel Buildings. American Institute of Steel Construction, USA, Chicago, IL, 2016.
[43] H.S. Lew, J.A. Main, S.D. Robert, F. Sadek, V.P. Chiarito, Performance of steel moment connections under a column removal scenario. I: experiments, J Struct Eng-ASCE 139 (1) (2013) 98–107.
[44] F. Dinu, I. Marginean, D. Dubina, Experimental testing and numerical modelling of steel moment-frame connections under column loss, Eng. Struct. 151 (2017) 861–878.
[45] H. Tang, X. Deng, Y. Jia, J. Xiong, C. Peng, Study on the progressive collapse behavior of fully bolted RCS beam-to-column connections, Eng. Struct. 109618 (2019) 199.
[46] T. Ngo, P. Mendis, A. Gupta, J. Ramsay, Blast loading and blast effects on structures – An overview. Electronic journal of structural engineering (EJSE), special issue: loading on Structures, 2007 76–91.
[47] H.M. Elsanadedy, T.H. Almusallam, Y.A. Al-Salloum, H. Abbas, Investigation of precast RC beam-column assemblies under column-loss scenario, Constr. Build. Mater. 142 (2017) 552–571.
[48] Y.A. Al-Salloum, M.A. Alrubaidi, H.M. Elsanadedy, T.H. Almusallam, R.A. Iqbal, Strengthening of precast RC beam-column connections for progressive collapse mitigation using bolted steel plates, Eng. Struct. 161 (2018) 146–160.
[49] T. Almusallam, Y. Al-Salloum, T. Ngo, P. Mendis, H. Abbas, Experimental investigation of progressive collapse potential of ordinary and special moment resisting reinforced concrete frames, Mater & Struct 50 (2017) 137.
[50] New Zealand Standard (NZS), Code of practice for general structural design and design loadings for buildings 1, NZS 4203: 1992, New Zealand.
[51] H. Jian, Y. Zheng, Simplified models of progressive collapse response and progressive collapse-resisting capacity curve of RC beam-column substructures, J. Perform. Constr. Facil. 28 (4) (2014), 04014008.
[52] O. Rashidian, R. Abbasnia, R. Ahmadi, F.M. Nav, Progressive collapse of exterior reinforced concrete beam–column sub-assemblages: considering the effects of a transverse frame, Int J Concr Struct Mater 10 (4) (2016) 479–497.
[53] ASTM, Standard test methods and definitions for mechanical testing of steel products. ASTM A370, vol. 16, American Society for Testing and Materials, West Conshohocken, PA, USA, 2016.
[54] CEN. EN 1993-1-5 Eurocode 3, Design of steel structures - Part 1–5: General rules - Plated structural elements, 2006 Brussels.
[55] Y. Bao, T. Wierzbicki, On fracture locus in the equivalent strain and stress triaxiality space, Int. J. Mech. Sci. 46 (1) (2004) 81–98.
[56] Arasaratnam P, Sivakumaran KS, Tait MJ. True stress-true strain models for structural steel elements. ISRN Civil Engineering Vol 2011, Article ID 656401, 11 pages.
[57] B. Meng, W. Zhong, J. Hao, Anti-collapse performances of steel beam-to-column assemblies with different span ratios, J Const Steel Res 140 (2018) 125–138.